

See discussions, stats, and author profiles for this publication at: <https://www.researchgate.net/publication/301759950>

Development of high crush efficient, extrudable aluminum front rails for vehicle lightweighting

Article in *International Journal of Impact Engineering* · April 2016

DOI: 10.1016/j.ijimpeng.2016.04.004

CITATIONS

37

READS

2,264

6 authors, including:



Christopher P Kohar

Rivian Automotive

22 PUBLICATIONS 220 CITATIONS

[SEE PROFILE](#)



Amir Zhumagulov

University of Waterloo

6 PUBLICATIONS 41 CITATIONS

[SEE PROFILE](#)



Abhijit Brahme

University of Waterloo

61 PUBLICATIONS 1,160 CITATIONS

[SEE PROFILE](#)



Kaan Inal

University of Waterloo

107 PUBLICATIONS 1,918 CITATIONS

[SEE PROFILE](#)

Some of the authors of this publication are also working on these related projects:



Sustainable Lightweighting Technologies: High Strength High Crush Efficiency Extruded Aluminum Front Rails For Lightweight Bodies [View project](#)



Modeling formability of FCC and HCP polycrystals using full-field spectral method based crystal plasticity model [View project](#)

Development of High Crush Efficient, Extrudable Aluminum Front Rails for Vehicle Lightweighting

Christopher P. Kohar¹, Amir Zhumagulov¹, Abhijit Brahme¹, Michael J. Worswick¹, Raja K. Mishra²,
Kaan Inal^{1*}

¹ Department of Mechanical and Mechatronics Engineering, University of Waterloo, Waterloo, ON, Canada,
N2L3G1

² General Motors Research & Development Center, Warren, MI, USA, 48090

Abstract

Understanding the behaviour of automotive structural components is essential for vehicle weight reduction and passenger safety. In this study, a novel framework is developed to design an optimized front rail that maximizes crash energy absorption characteristics. The new design is coupled with material and process development to provide a component with superior energy absorption and strength characteristics that is commercially sustainable. Simulations of the extrusion crush behaviour are performed using the anisotropic Barlat *et al.* (2003) Yld2000 yield functions. The simulations are compared to the dynamic crush results for this extrusion. The size of the structure is optimized using the response surface methodology, using artificial neural networks metamodels and simulated annealing optimization techniques. The specific energy absorption (SEA) is used as a single optimization objective function for maximizing energy absorption and minimizing mass. An analytical relationship that relates the SEA function to the crush efficiency is derived to show that a single optimization function parameter may be sufficient for mass minimization. Analysis is performed to identify key extrusion operational parameters and the wall thickness is identified as the most important parameter to control during extrusion.

Keywords: Aluminum; crush tubes; optimization; crashworthiness.

* Corresponding Author. Tel: +1 519 888 4567 Ext. 38114. Fax: +1 519 885 5862. Email Address: kinal@uwaterloo.ca

1 Introduction

Implementation of lightweight aluminum alloys to fabricate automotive components has become integral to achieve vehicle mass reduction. Major energy absorption structures of automobiles, such as the front rails, rockers, pillars, etc. are excellent candidates for mass reduction with aluminum because they contribute substantially to the overall vehicle weight. Such components must be designed to exhibit energy dissipation comparable to that of current steel components in the event of a collision to meet vehicle safety requirements [1].

The crush behaviour of lightweight structures has been a widely studied topic in literature for several decades. Initial work by Wierzbicki, Abramowicz, and Jones led to the development of mechanics of axial crush based on analytical models that closely reflected experimental data for steel components [2, 3, 4, 5, 6, 7, 8, 9, 10, 11]. With improvements in computational technology over time, commercial non-linear finite element packages, such as LS-DYNA, have been utilized to predict the energy absorbing response of complex structures from other materials. Langseth *et al.* [12, 13] used commercial finite element software to simulate and validate the quasi-static and dynamic crush response of aluminum extrusions using an isotropic von Mises hardening model. They compared their simulation results with experimental crush data from various aluminum structures and found good agreement. Kim [14] combined experimental observations and finite element results to manually optimize the topology of a single piece multi-cellular aluminum extrusion. Mayer *et al.* [15] explored the effects of artificial aging to improve the quasi-static crush behaviour of multi-cell extrusions from AA6061 and AA6063 aluminum alloys. They observed that after a specific aging time, the crush performance of the AA6063 structure remained unchanged at an optimal performance.

In recent years, the use of optimization software that utilizes artificial intelligence and machine learning algorithms has served as a valuable tool in improving the crashworthiness performance (see e.g. [16, 17, 18, 19, 20, 21, 22, 23]). Multiple finite element simulations have been performed on the axial crush response of the structures using isotropic hardening models. Mathematical models have been

developed to predict the crash response of finite element simulations as a function of input parameters. Machine learning and optimization techniques have been applied to such models to increase the crash performance by varying the topology and topography of the structure. This approach, known as structural optimization through the response surface methodology [24], has been employed to optimize the shape of honeycomb structure to maximize the energy absorption [25]. Esfahani *et al.* [25] have used numerous finite element simulations to calibrate a mathematical model and perform optimization using a hybrid-adaptive simulated annealing algorithm. Through this technique, they have been able to optimize the energy absorption of the structure, while minimizing mass.

Currently commercially available 7xxx series aluminum alloys have very high specific strength that is comparable to that of steel and allow for easy substitution for conventional steel applications. The main drawbacks of 7xxx series alloys continue to be their poor corrosion resistance, low extrudability leading to high cost and recycling limitations in multi-material vehicle applications. From consideration of the extrudability and recycling, the 6xxx series alloys are superior to 7xxx series for mass-production application. However, the 6xxx series alloys have a lower specific strength compared to the 7xxx series alloys. A technological platform capable of optimizing the shape of the profile to meet energy absorption requirements with the lower strength 6xxx extrusion is presented in this study.

An aluminum extrusion profile with multi-cellular structure as a crush structure is an excellent candidate for further optimization because the wall thickness – a parameter that strongly correlates with mass as well as energy absorption - can be easily controlled and varied in the manufacturing process. A multi-cavity extruded tube made from an AA7xxx alloy that satisfies the design constraints and meets the crush energy absorption needs for front rail applications in a current production vehicle is then taken as a benchmark for optimization of 6xxx structure in this investigation. The benchmark tube is experimentally crush tested using a dynamic sled apparatus to obtain the experimental energy absorption response. AA6063-T6 extrusion with the same profile is crushed under the same experimental conditions for comparison. The commercial FE software, LS-DYNA, is used to simulate the crush behaviour of the

AA6063-T6 structure using measured material anisotropy and high strain rate behaviour data from the extruded tubes as input. The simulation results are compared to experimental results to validate the FE model. New multi-cellular extrusion profiles are developed through FE modeling, manufactured, sled-tested and crush simulation results are compared with experiments. The size of the new multi-cellular extrusion is optimized using the response surface methodology, to further improve the energy absorption characteristics, while the topology and topography is held constant. The sizing of the extrusion is varied using the commercial optimization package, LS-OPT. The specific energy absorption, which maximizes the energy absorption and minimizes the mass, is selected and evaluated as a single optimization objective.

2 Experiments

Figure 1 presents the cross-section of the baseline extrusion profile. Commercially available AA6063 billets were extruded using a commercial extrusion press and the extruded rails were artificially aged to a T6-temper. Figure 2 shows a new multi-cellular four-cell hexagon structure, referred to as UWR4 extrusion profile, which was also extruded. The multi-cellular topology was developed through an optimization of the number of crush elements within the profile envelop (for further details on this approach, the readers are refer to Ref [25, 14, 26]). Each aluminum extrusion profile was cut to a length of 464mm for crush experiments. Table 1 presents the length, mass and other data for the tested materials. Table 2 lists the chemical composition of the extruded tubes.

Quasi-static uniaxial tensile tests, in accordance with ASTM-E8, were performed using specimens cut along the extrusion direction of the baseline profile to explore the variation in the mechanical behaviour in eleven different locations (as indicated in Figure 1). The resulting true stress-true strain curves are shown in Figure 3. Some variation existed in the T6-temper mechanical responses. In particular, two stress-strain responses exceeded the average response, due to the variation in the cooling

rate of the internal webs (numbered 7 and 9 in Figure 1) during the extrusion process. An average stress response was fit to a power-law hardening model [27]:

$$\bar{\sigma} = K(\varepsilon_0 + \bar{\varepsilon}_p)^n \quad (1)$$

where $\bar{\sigma}$ is the effective yield stress, $\bar{\varepsilon}_p$ is the total plastic strain, ε_0 is the total elastic strain, K is the strength coefficient and n is the work hardening exponent. Table 3 lists the representative parameters.

In the experimental work of Hsu and Jones [28] for extruded AA6063-T6, it was reported that this alloy exhibits moderate strain rate sensitivity. Thus, moderate strain rate tensile testing was performed for strain rates of 10/s and 100/s. Miniature dog-bone specimens were cut from the extrusion and pulled in uniaxial tension using a hydraulic intermediate strain rate apparatus. The details about the experimental apparatus and testing procedure are similar to that described in Bardelcik *et al.* [29]. The power law plasticity relation, coupled with the Cowper-Symonds strain rate sensitivity [30], was used to characterize the strain-rate sensitivity. This relates the effective stress, $\bar{\sigma}$, to the total plastic strain, $\bar{\varepsilon}_p$, and it is written as

$$\bar{\sigma} = K(\varepsilon_0 + \bar{\varepsilon}_p)^n \left(1 + \left(\frac{\dot{\varepsilon}}{M} \right)^{\frac{1}{P}} \right) \quad (2)$$

where M is the reference material strain-rate sensitivity coefficient and P is the strain-rate sensitivity exponent. Strain rate sensitivity parameters of $M = 5.60 \times 10^{10} s^{-1}$ and $P = 12.6$ were calibrated to the moderate strain rate data presented in Figure 4. These values compare well with the experimental values obtained from the work of Hsu and Jones [28] for extruded AA6063-T6, ($M = 9.39 \times 10^{10} s^{-1}$ and $P = 9.55$).

A schematic of the dynamic crush experimental setup is shown in Figure 5. The aluminum extrusions were clamped between steel boss structures and impacted using a sled-track apparatus. Only one profile was tested at a time. The mass of the sled was 855kg and the impacting speed was 8.00 m/s

[28.8km/h]. No crush triggers were used for any of the dynamic tests. A 12.7mm [0.50"] plywood sheet was mounted to the end plate to minimize the high frequency noise from the metal-to-metal contact. Aluminum honeycomb blocks were used to dissipate any excessive sled energy in the event of an unforeseen catastrophic failure of the crush tube. This setup provided for a free-crush length of 125mm for each extrusion before the sled-mass would impact the aluminum honeycomb blocks.

Figure 6 shows the experimental force-displacement and energy absorption response of the tubes from the dynamic crush experiments. The force-displacement response had several oscillations in the response, attributed to the structural vibrations of the sled-track setup [31]. To attenuate the noise, the raw dynamic force-displacement response was post-processed using a SAE CFC 180 filter. The total energy absorption, E_{abs} , is calculated by integrating the force-displacement response for the free-crush distance, L , of 125mm, such that

$$E_{abs} = \int_0^L F(x)dx \quad (3)$$

The mean crush force, F_{mean} , is calculated by averaging the absorbed energy over the crush distance, such that

$$F_{mean} = \frac{1}{L} \int_0^L F(x)dx \quad (4)$$

The peak crush force, F_{peak} , is measured as the highest value of crush force exerted, which was typically observed at the initial instant of impact. The crush efficiency, η , is defined as the ratio of the mean crush force and the peak crush force [32]

$$\eta = \frac{F_{mean}}{F_{peak}} \quad (5)$$

Figure 7 shows the experimental crushed tubes for each profile. Each experimental crush tube produced a combination of Type-I crush modes during crush [10]. Table 4 lists a summary of the energy absorption, mean crush force, peak crush force, and the crush efficiency at different velocities. The mean

crush force values of the baseline AA7xxx, baseline AA6063-T6, and UWR4 AA6063-T6 profile are 171.4kN, 92.5kN, and 121.9kN respectively. At 125mm crush distance, the baseline 7xxx Series, baseline AA6063-T6, and UWR4 AA6063-T6 absorbed 20.6kJ, 11.0kJ, and 14.6kJ of energy respectively. The peak crush force values for respective profile are 255.4kN, 161.4kN and 190.0, corresponding to a crush efficiency of 67.1%, 57.3% and 64.2%, respectively. The UWR4 AA6063-T6 tube had a higher mean crush force and energy absorption than the baseline AA6063-T6 tube. Although the peak crush force of the UWR4 AA6063-T6 was higher than that of the baseline AA6063-T6, its crush efficiency was higher. Thus, the UWR4 structure had a superior crush performance than the baseline structure. The Baseline AA7xxx tube had the best crush performance, but it also had the most mass. Therefore, the energy absorption characteristics of the UWR4 needs to be further optimized by varying mass as well as material properties attainable in AA6xxx series alloys to replace the AA7xxx extrusions.

3 Constitutive Model

As shown in the work by Kohar *et al.* [33], both the effects of Lankford coefficients and the yield stress as a function of orientation have a significant effect on simulation predictions of the energy absorption characteristics. This was shown using the advanced CPB06ex2 yield function, which could capture both the Lankford coefficients and yield stresses [34]. They found that the Lankford coefficients had a larger influence on the final energy absorption compared to the yield stress anisotropy. The goal of this study is to demonstrate the influences of capturing the anisotropy using a simple anisotropic yield function, such that the computational time is minimal. The Barlat and Lian (1989) [35] yield function is able to capture the variation of the Lankford coefficients, but does not capture the yield stress variation. As observed both by Jansson *et al.* [36] and Achani *et al.* [37], extruded aluminum alloy AA6063 has a larger Lankford variation than the yield stress variation with respect to the extrusion direction. Using the simple Barlat and Lian (1989) yield function can over emphasize the yield stress variation because it is not directly captured in the yield function. In Achani *et al.* [37], the Yld2000 and Yld2004 yield functions

by Barlat *et al.* [38, 39] were evaluated for their applicability for extruded aluminum alloy AA6063-T6. They found that the Yld2004 yield function captured the anisotropy better than the Yld2000 yield function. However, the Yld2004 yield function required 18 parameters to calibrate the yield function, as opposed to the 8 parameters required for the Yld2000 yield function. Furthermore, the Yld2004 yield function requires individual linear stress transformations to be computed, which requires significantly more computational resources. Therefore, the Barlat *et al.* [38] Yld2000 yield criterion is employed through this study because it has good predictive capability with reasonable computational efficiency.

Yld2000 constitutive model [38] is utilized as *MAT_133 (*MAT_BARLAT_YLD2000) in LS-DYNA. The plane stress yield function is defined as [38]

$$\Phi_{YLD2000} = \phi' + \phi'' - 2\bar{\sigma}^a = 0 \quad (6)$$

where $\bar{\sigma}$ is the effective yield stress and ϕ' and ϕ'' are anisotropic functions that are linearly transformed, such that

$$\phi' = |X_1' - X_2'|^a \quad \phi'' = |X_1'' + 2X_2''|^a + |2X_1'' + X_2''|^a \quad (7)$$

where X_i' and X_i'' are the principal stresses of the linearly transformed Cauchy stress tensor, $\boldsymbol{\sigma}$. The transformed stress state is defined as

$$\mathbf{X}' = \mathbf{L}' \cdot \boldsymbol{\sigma} \quad \mathbf{X}'' = \mathbf{L}'' \cdot \boldsymbol{\sigma} \quad (8)$$

where the \mathbf{L}' and \mathbf{L}'' are linear stress transformation tensors defined as

$$\mathbf{L}' = \begin{bmatrix} L_{11}' & L_{12}' & 0 \\ L_{21}' & L_{22}' & 0 \\ 0 & 0 & L_{66}' \end{bmatrix} \quad \mathbf{L}'' = \begin{bmatrix} L_{11}'' & L_{12}'' & 0 \\ L_{21}'' & L_{22}'' & 0 \\ 0 & 0 & L_{66}'' \end{bmatrix} \quad (9)$$

Such that

$$\begin{bmatrix} L_{11}' \\ L_{12}' \\ L_{21}' \\ L_{22}' \\ L_{66}' \end{bmatrix} = \begin{bmatrix} 2/3 & 0 & 0 \\ -1/3 & 0 & 0 \\ 0 & -1/3 & 0 \\ 0 & 2/3 & 0 \\ 0 & 0 & 1 \end{bmatrix} \begin{bmatrix} \alpha_1 \\ \alpha_2 \\ \alpha_7 \end{bmatrix} \quad \begin{bmatrix} L_{11}'' \\ L_{12}'' \\ L_{21}'' \\ L_{22}'' \\ L_{66}'' \end{bmatrix} = \frac{1}{9} \begin{bmatrix} -2 & 2 & 8 & -2 & 0 \\ 1 & -4 & -4 & 4 & 0 \\ 4 & -4 & -4 & 1 & 0 \\ -2 & 8 & 2 & -2 & 0 \\ 0 & 0 & 0 & 0 & 9 \end{bmatrix} \begin{bmatrix} \alpha_3 \\ \alpha_4 \\ \alpha_5 \\ \alpha_6 \\ \alpha_8 \end{bmatrix} \quad (10)$$

The principal transformation stress for the first transformed plane stress state, $X_{1,2}'$, is determined as

$$X_{1,2}' = \frac{1}{2} \left(X_{xx}' + X_{yy}' \pm \sqrt{(X_{xx}' - X_{yy}')^2 + 4X_{xy}'} \right) \quad (11)$$

A similar formulation is defined for the second transformed stress state, $X_{1,2}''$. The coefficient a is an exponential hardening coefficient that is a function of the crystal structure. For face centered cubic material, such as aluminum, $a = 8$ [40]. The parameters α_i are determined by fitting the yield stress and Lankford coefficients at the balanced biaxial strain path, three Lankford coefficients and three yield stress variation with respect to the extrusion direction. The Lankford coefficients, $R_{00}, R_{45},$ and R_{90} , are satisfied through the following relation [41]

$$R_\theta = \frac{d\varepsilon_{22}(\theta)}{d\varepsilon_{33}(\theta)} = - \frac{\sin^2 \theta \frac{\partial f(\theta)}{\partial \sigma_{11}} - \sin(2\theta) \frac{\partial f(\theta)}{\partial \sigma_{12}} + \cos^2 \theta \frac{\partial f(\theta)}{\partial \sigma_{22}}}{\frac{\partial f(\theta)}{\partial \sigma_{11}} + \frac{\partial f(\theta)}{\partial \sigma_{22}}} \quad (12)$$

where $\sigma_{11} = \cos^2 \theta$, $\sigma_{12} = \sin \theta \cos \theta$, $\sigma_{22} = \sin^2 \theta$ and θ is the orientation with respect to the extrusion direction. The yield stress variation is $\sigma_{00}, \sigma_{45}, \sigma_{90}$ and the balanced biaxial yield stress, σ_b , are satisfied through Equation (6). The balanced biaxial Lankford coefficient is given by

$$R_b = \frac{d\varepsilon_{22}(\sigma_{11} = \sigma_{22} = \sigma_b)}{d\varepsilon_{11}(\sigma_{11} = \sigma_{22} = \sigma_b)} = \frac{\frac{\partial f(\sigma_{11} = \sigma_{22} = \sigma_b)}{\partial \sigma_{22}}}{\frac{\partial f(\sigma_{11} = \sigma_{22} = \sigma_b)}{\partial \sigma_{11}}} \quad (13)$$

This provides eight non-linear equations and eight unknowns, which is solved using the Newton-Raphson method. The experimental anisotropy parameters (Lankford Coefficients) and yield stress variations for extruded AA6063-T6 given by Achani *et al.* [37], are used in this study. Figure 8 presents the normalized (about x-direction) yield surface calculated using the above data. The isotropic von Mises yield surface is also presented for comparison.

4 Finite Element Modeling

The axial crushing response of extruded tubes of the baseline AA6063-T6 and UWR4 AA6063-T6 were simulated using a finite element (FE) model. A non-linear explicit dynamic formulation available in the commercial LS-DYNA software FE code was used throughout this work [27]. The FE models for

the two profiles are shown in Figure 9 and Figure 10. The FE mesh was generated using the commercial meshing software Altair Hyperworks Hypermesh. The FE model setup and comparison with experiments are presented and discussed below and is similar to the approach described by Kohar et al. [31].

The FE model consists of the crush tube constrained between two steel bosses. Each crush tube was meshed about the mid-thickness of the profile geometry, which are presented in Figure 1 and Figure 2. Each of the five unique wall thickness sections (shown in red, blue, brown, magenta and cyan) were individually meshed. The top (yellow) and bottom (green) boss fixtures were individually meshed according to the experimental setup requirements.

The top boss was assigned a mass of 855kg by modifying the density of steel. The top boss was constrained axially in the z-direction and was given an initial velocity of 8m/s. The base boss fixture was constrained in all degrees of freedom on the bottom face. A total simulation time of 30 milliseconds was used for this study. The force-displacement response of the top embossment was monitored to obtain the energy absorption characteristics. The elastic material properties are listed in Table 6.

The steel bosses were modeled as an elastic material. Eight-node brick elements with full selective reduced integration were used to model these components. A mesh size of $2.00\text{mm} \times 2.00\text{mm} \times 2.00\text{mm}$ was employed for the bosses. A 6mm region was meshed around the outside of the crush tube to simplify the model. The crush tube was meshed using Belytschko-Tsay shell elements to simulate plane stress deformation. A mesh size of $2.00\text{mm} \times 2.00\text{mm}$ with 7 through thickness integration points was employed through the crush tube. As presented in Kohar *et al* [33], contact algorithms are placed between the crush tube and the rigid plates to capture the friction of the crush tube folds against the bosses. The static and dynamic coefficients of friction were set to 0.45 and 0.40 respectively. Self-contact algorithms were also placed to capture the effects of the folds stacking onto each other. Accordingly, the static and dynamic coefficients of friction for this contact were set to 1.04 and 1.00 respectively [42, 43].

4.1 Comparison of experiment with simulation

Figure 11 presents the predicted effective plastic strain contours for the Baseline Profile – AA6063-T6 and UWR4 – AA6063-T6. The folding patterns of each simulation show good agreement with the experimental deformation. Figure 12 presents the force-displacement and energy absorption predications for each profile that was simulated. Each force-displacement response was filtered using a SAE CFC 180 filter. Table 7 and Table 8 presents the predicted mean crush force, energy absorption, peak crush force and crush efficiency for each respective simulated profile. The error, denoted as ΔErr , between the simulation prediction and experiment for each simulated profile is also presented in Table 7 and Table 8. The error for the Baseline AA6063-T6 mean crush force, peak crush force, energy absorption, and crush efficiency was 7.6%, 5.9%, 2.7%, and 1.0% respectively. The error for the UWR4 AA6063-T6 mean crush force, peak crush force, energy absorption, and crush efficiency was 0.0%, 2.9%, 0.0%, and 1.9% respectively. The overall trend of the force-displacement response and energy absorption-displacement response show good agreement with each experiment. Since the model has good predictive capabilities, it is concluded that the FE model has been constructed properly and is suitable for size optimization.

5 Front Rail Optimization Strategy for Thickness

In this section, the framework for the Front Rail Optimization Strategy of Thickness (FROST) Method is detailed. The FROST Method is a numerical framework that was implemented to optimize the size of the UWR4 crush rail. The commercial optimization package LS-OPT was used to perform the optimization procedure.

5.1 Framework for Optimization Method

For the optimization of the crush tube, the FROST method begins by decomposing the geometry into individual parts. As shown in Figure 10a, the UWR4 crush tube is individually meshed into five unique parts that are composed of shell elements and constrained together. The overall topology is held constant and the size of the structure is optimized. In other words, the focus of the work is constrained to

optimizing the thickness of the structure. Each component is assigned its own unique part identification, material and shell element sectional information. Thus, the shell element thickness for each section is parameterized accordingly as t_i with $i = 1 \dots 5$. Sets of parameters within this space, which is known as the design of experiments [24], are selected for simulation. Using a linear space filling point selection algorithm, 10 sample sets of thickness combinations (t_i) are selected within these bounds and each combination is simulated. For each set of parameters, the resulting mass and mean crush force is measured and is used as the performance metric for optimization. The optimization function, optimization strategy and constraints are discussed further below.

5.1.1 Optimization Objective Function

The objective of this optimization is to minimize the mass while maximizing the mean crush force. To evaluate each design, a performance metric, P , must be defined that can encapsulate this objective

$$P(t_i) = f\left(\frac{F_{mean}}{Mass}\right) \quad (14)$$

Since the topology of the structure is fixed and must remain as an extrusion, an approximate linear functional constraint is imposed on the mass of the structure (when neglecting the radii), such that

$$Mass = L\rho \sum_{i=1}^5 a_i t_i \quad (15)$$

where a_i is dependent on the dimensions of the section of the structure and L is the initial uncrushed length. In the work by Wierzbicki and Abramowicz [10], a formulation that related the kinematic deformations to the energy absorption capabilities in simple Type-I collapse modes using an isotropic rigid-perfectly plastic material behaviour was presented

$$E = \frac{f(\sigma)t^2}{4} \left(16HI_1 \frac{b}{t} + 2\pi C + 4I_3 \frac{H^2}{b} \right) \quad (16)$$

265 where I_1, I_3 are constants, V is the impacting velocity, $f(\sigma)$ is the material yield stress function, C is the
 266 macro element length and t is the material thickness. H and b are geometric constants, dependent on t ,
 267 that naturally minimizes the energy absorption capabilities of the structure, such that

$$\frac{\partial E}{\partial H} = 0, \frac{\partial E}{\partial b} = 0 \quad (17)$$

268 For a perfectly plastic material with rate sensitivity, the material yield stress function is described as

$$f(\sigma) = \sigma_0 \left(1 + \left(\frac{V}{3CM} \right)^{\frac{1}{P}} \right) \quad (18)$$

269 where V is the impacting velocity [5] and σ_0 is the yield stress. By dividing by the total crushing distance,
 270 δ , the mean crush force can be determined as

$$F_{mean} = \frac{E}{\delta} = \frac{f(\sigma)t^2}{4\delta} \left(16HI_1 \frac{b}{t} + 2\pi C + 4I_3 \frac{H^2}{b} \right) \quad (19)$$

271 Since the crush tube consists of a combination of Type-I collapse elements, this means that the mean
 272 crush force response of this crush tube will be at least functionally quadratic with respect to material
 273 thickness. The specific energy absorption (SEA) is a common performance metric that is used for
 274 evaluating the performance of a crush tube [14]

$$SEA = \frac{E}{Mass} = \frac{F_{mean}\delta}{Mass} \quad (20)$$

275 Evaluating the performance metric at a given crush displacement, the first performance metric is defined
 276 as

$$P_1(t_i) = SEA = \frac{E}{Mass} = \frac{F_{mean}\delta}{Mass} = \frac{\delta\sigma_0}{4L\rho} \sum_{i=1}^5 \frac{t_i^2 \left(16H_i I_1 \frac{b_i}{t_i} + 2\pi C_i + 4I_3 \frac{H_i^2}{b_i} \right) \left(1 + \left(\frac{V}{3C_i M} \right)^{\frac{1}{P}} \right)}{a_i t_i} \quad (21)$$

277 where i denotes a section of the profile. This performance metric is a linear function with respect to the
 278 wall thickness, t_i , to a first order with a contribution of higher order non-linear functions. Since the

279 structure is a combination of multiple Type-I collapse elements, the objective function will attempt to
 280 optimize the section where the local SEA has the greatest influence.

281 As presented in the work of Marzbanrad *et al.* [19], there are other choices available as an
 282 optimization objective function. Another common performance metric, $P_2(t_i)$, is to optimize the crush
 283 efficiency of the structure, such that

$$P_2(t_i) = \eta = \frac{F_{mean}}{F_{peak}} \quad (22)$$

284 In the work of Kohar *et al.* [26], it was shown that the peak crush response of Type-I collapse elements is
 285 linearly proportional to the area of the structure and the flow stress properties of the material

$$F_{peak} \propto Af(\sigma) \quad (23)$$

286 Since the topology and the material properties of the extrusion is fixed, the peak force becomes linearly
 287 functional, such that

$$F_{peak} = f(\sigma) \sum_{i=1}^5 a_i t_i \quad (24)$$

288 Thus, the performance metric for optimizing the crush efficiency takes the form

$$P_2(t_i) = \eta = \frac{F_{mean}}{F_{peak}} = \frac{1}{4} \sum_{i=1}^5 \frac{t_i^2 \left(16H_i l_1 \frac{b_i}{t_i} + 2\pi C_i + 4l_3 \frac{H_i^2}{b_i} \right)}{a_i t_i} \quad (25)$$

289 This performance metric is also to a first order linear function of wall thickness with a contribution of
 290 higher order non-linear functions that maximizes the crush force and minimizes the mass.

291 With two different performance metrics, another method is to develop a multi-objective
 292 performance metric, P_3 , that is a weighted sum of the individual performance metrics

$$P_3(t_i) = w_1 SEA + w_2 \eta \quad (26)$$

293 where w_i are individual weights assigned to each parameter. This function is able to not only capture the
 294 desired weight minimization, but capture the benefit of optimizing the crush efficiency. However, from

the above derivations, the specific energy absorption and crush efficiency have the same functionality. In fact, it is proposed that the specific energy absorption and crush efficiency are directly proportional to each other through Υ , such that

$$\Upsilon = \frac{P_2(t_i)}{P_1(t_i)} = \frac{\eta}{SEA} = \frac{\rho L}{\delta f(\sigma)} \quad (27)$$

For an isotropic power law hardening material, the equivalent perfectly plastic yield stress can be determined as [44]

$$\sigma_0 = \sqrt{\frac{\sigma_y \sigma_u}{n+1}} \left(1 + \left(\frac{V}{3C_i M} \right)^{\frac{1}{p}} \right) \quad (28)$$

where σ_y is the yield stress and σ_{uts} is the ultimate tensile strength. Substituting into the multi-objective optimization function produces

$$P_3(t_i) = \left(w_1 + w_2 \frac{\rho L}{\delta f(\sigma)} \right) SEA \quad (29)$$

It can be concluded that when optimizing the specific energy absorption, the crush efficiency is also optimized. Therefore, it is proposed that selecting only a single objective optimization function is required for minimizing weight and maximizing energy absorption. In this work, the specific energy absorption is selected as the optimization objective function.

5.1.2 Optimization Strategy

The response surface method (RSM) was used to develop a metamodel for the optimization of the performance metric [24] [45]. A metamodel is a mathematical model that is used to relate input functions to an output function through minimization of statistical error. Some common metamodeling techniques use a polynomial regression method [20] or neural networks [46] to generate the input-output response for structural optimization. In this application, a metamodel was created that relates the set of material thickness for the structure to the performance metric. Once the metamodel was been created, it could be used to predict the output response of the simulation. A feed-forward multi-layered neural-network, with

a single hidden layer, was implemented as the metamodeling technique to map the material thickness because it provides sufficient complexity to approximate the input-output relationship [47].

Once the metamodel has been generated, an optimization algorithm operates on this function to generate the optimal parameters for the optimization objective. An adaptive simulated annealing (ASA) algorithm was used to perform the optimization procedure on the neural network generated metamodel [48, 49, 50]. The optimization objective consists of a complex trade-off objective function that is highly constrained, which is very well suited for the ASA method [50]. Upon determining an initial optimal solution, a new subspace within the design is generated within the previous design space using the sequential response surface method (SRSM). The new region is generated to encompass the current optimal solution through an adaptive contraction and panning window that are designed to alleviate oscillation and prevent premature convergence [51]. Further iterations and domain reductions are performed until a local optimal solution is obtained for the given problem. This method assures that a local optimal solution is obtained. However, this solution is highly dependent on the accuracy of the metamodel, such that initial domain reductions may exclude a region where better performance could be obtained. This response surface methodology and optimization process was performed using LS-OPT.

5.1.3 Optimization Criteria and Constraints

Several criterion and constraints were placed on the optimization process:

1. An upper and lower bound of 2.40mm and 1.75mm respectively was placed on each thickness parameter to generate UWR4 crush rails that were feasible for extrusion. The lower limit was selected as the lowest extrudable wall thickness for the given size of the profile. The upper limit was determined by limiting the variation of wall thickness to not exceed 40% above the lower limit. The constraints on these design parameters constitute what is commonly known as the design space. Each parameter could vary in discrete increments of 0.01mm.

2. A convergence error, $Err_{converge}$, constraint of 0.01 was imposed on the neural network to ensure that metamodel has predictive capabilities. This means that the error between the predicted output of the metamodel to the actual output of the simulation for the given input (thickness) parameters must be less than 1%.
3. Newly synthesized topographies should have the same or better performance than the Baseline 7xxx series shape (presented in Figure 1). A newly generated UWR4 crush rail should have a mass less than 1.494 kg and a crush force greater than 171.0kN. If both criteria cannot be satisfied simultaneously, preference was given to satisfying the mass criteria.

The optimization problem of the sizing for the UWR4 crush can be formulated as follows:

$$\left\{ \begin{array}{l} \text{Max } \{SEA(t_i)\} \\ \text{s.t. Mass} \leq 1.494 \text{ kg (strict)} \\ F_{mean} \geq 171.0 \text{ kN} \\ t_i \in [1.75, 1.76, \dots, 2.40] \text{ mm} \\ Err_{converge} \leq 0.01 \end{array} \right. \quad (30)$$

5.2 Optimization Analysis

The FROST Method was applied to the 8.0m/s explicit dynamic FE model using an isotropic plasticity model (*MAT_LINEAR_PIECEWISE_PLASTICITY). This reduced computational resources required to navigate throughout the design of experiments domain. Once the FROST Method converged to an optimal isotropic solution, a final simulation of the new superior UWR4 sizing was performed using the Yld2000 anisotropic yield function. A sensitivity analysis was performed to identify an operation window for the extrusion tolerances of the new UWR4 profile.

5.2.1 Results of Optimization

APPENDIX A presents the test matrix that details the simulation parameters. The energy absorption characteristics of each size combination was measured and also presented in APPENDIX A. Figure 13 presents the convergence history for each thickness parameter using the isotropic model. The wall thickness for each section specified in Figure 2 was used as an initial guess of the optimal sizing. A

residual error function, $r_j(t_i^{(\alpha)})$, is defined that represents the error between the metamodel response, $g_j(t_i^{(\alpha)})$, and the actual measured value from the simulation, $y_j(t_i^{(\alpha)})$ for a given set of independent coefficients at the current iteration $t_i^{(\alpha)}$. The residual error function can be written as;

$$r_j(t_i^{(\alpha)}) = y_j(t_i^{(\alpha)}) - g_j(t_i^{(\alpha)}), \quad i = 1, \dots, 5, \quad j = 1, \dots, m \quad (31)$$

where α is the current iteration and m is the number of total simulations at the given iteration. The accuracy of the metamodel is determined by calculating the average error for each simulation. The average error between the simulation results and the model formulations is defined in as

$$\overline{Err} = \frac{1}{m} \sum_{i=1}^m \frac{|r_i|}{y_i} \times 100\% \quad (32)$$

where m is the number of sample points. Figure 14 presents the convergence history of the metamodel response of the SEA function. Furthermore, Figure 15 presents the convergence history of the optimal SEA that satisfies the design constraints. These figures show that the predictive error between the metamodel and direct simulations and optimal direction simulation is 0.57% and 0.30% respectively. Table 9 presents the initial and final dimensions and mass for the UWR4 model. The isotropic optimization process required a total of 7 iterations to converge to its final configuration. The final mass of the structures converged to a mass of 1.494kg, which corresponds to the limit of the allowable mass constraint imposed. This is a result of SEA being dominant by first order linear functions of wall thickness as presented in Equation (19) [4].

A plot of the SEA response surface and contours for the isotropic process are presented in Figure 16. Each plot is centered about the final converged set of parameters. The maximum allowable mass limit is imposed on each figure in black. This line indicates the combinations of two parameters that produced a mass of 1.494kg. The final wall thickness configuration from the optimization procedure is also presented in each figure. These figures show that decreasing the mass tends to decrease the SEA of the structure. Again, this is a result of the SEA being dominant by first order linear functions (with higher order terms)

of wall thickness. Thus, the optimization objective of maximizing SEA will tend to converge towards the limit of the mass constraints.

5.2.2 Interaction of Specific Energy Absorption and Crush Efficiency

Figure 17 presents the specific energy absorption and the crush efficiency results obtained from each simulation during the isotropic optimization process. Each point, shown as a red square with a black box, represents the SEA and crush efficiency for a given point in the design of experiments. Table 10 presents a simple linear regression that is plotted through this data. The R^2 value for the regression fit is 0.6013. This means that there is a moderate positive linear relationship between the specific energy absorption and the crush efficiency. Equation (27) was evaluated and also presented in Table 10 to determine analytical relationship between the specific energy absorption and the crush efficiency. Equation (27) was calculated using an ultimate tensile strength calculated at 100% plastic strain ($\sigma_{uts}|_{\bar{\epsilon}_p=1} = 310MPa$). Since energy absorption is naturally minimized by the structure, the effects of strain rate are calculated by minimizing Equation (28) with respect to the geometry, where C_i is calculated as the average macro element length [10]. The difference between the analytical parameter and the regression fit for the isotropic models is 6.7%. This means that, using the isotropic material model, one can directly calculate the crush efficiency of the structure once the specific energy absorption is known. Since the optimization process is guided towards the largest allowable mass, the resulting maximization of the specific energy absorption results will tend to simultaneously increase the maximization of the crush efficiency.

5.2.3 Optimized Anisotropic UWR4 Simulation Results

Figure 18 presents the simulated force-displacement and energy absorption response of the new UWR4 sizing using the Yld2000 anisotropic yield function. Table 11 presents a summary of the energy absorption characteristics of the new UWR4 profile. The mean crush force, peak crush force, energy absorption and crush efficiency was 148.6kN, 248.9kN, 18.5kJ, and 59.7% respectively. Although the mass constraint was satisfied, the mean crush force criteria was not. Even though a 2.5% decrease in the

crush efficiency is observed, the new UWR4 profile has 26.7% more energy absorption and a higher crush force by 21.9% than the initial UWR4 profile when increasing the mass by 21%. Although the mean crush force and energy absorption is 10% and 13% respectively lower than the Baseline 7xxx Series profile, the new UWR4 profile can achieve comparable energy absorption characteristics for the given mass using the AA6xxx-T6 alloy of appropriate strength.

5.2.4 Size Sensitivity Analysis

Figure 19 presents a wall thickness sensitivity analysis for the mean crush force, mass, and SEA of the new UWR4 AA6063-T6 profile. The gradient of each response, β_i , is calculated using a first order regression, such that

$$\text{a) } \beta_o = (\mathbf{X}^T \mathbf{X})^{-1} \mathbf{X}^T F_{mean} \quad \text{b) } \beta_1 = (\mathbf{X}^T \mathbf{X})^{-1} \mathbf{X}^T Mass \quad \text{c) } \beta_2 = (\mathbf{X}^T \mathbf{X})^{-1} \mathbf{X}^T SEA \quad (33)$$

where $\mathbf{X} = [t_1, t_2, t_3, t_4, t_5]$. The first order approximation is appropriate to represent the approximation of SEA, which is the primary optimization goal. This analysis shows that mean crush force and mass was most sensitive to the wall thickness Parameter t_3 . However, Parameter t_4 had the highest sensitivity to SEA. Parameter t_1 had the lowest sensitivity to the mean crush force and the second lowest sensitivity to any mass increase. As a result, the overall SEA sensitivity to Parameter t_1 was the lowest of all parameters, followed by Parameter t_2 . It also shows that Parameters t_5 and t_3 followed after t_4 in order of SEA sensitivity. This was reflected in the convergence history of Figure 13, where Parameters t_4 and t_5 converged to the limit of the bounds. Parameters t_1 and t_2 converged to the lowest combination that produced the largest mass, which produced the largest SEA. Thus, higher quality extrusion process control should be applied to Parameter t_4 to ensure the crush structure absorbs energy in the most efficient manner.

6 Conclusion

In this paper, a framework was presented for optimizing the sizing of a multi-cellular aluminum extrusion for automotive crashworthiness applications. New AA6063-T6 aluminum extrusion profiles

were designed using finite elements, fabricated and dynamically crushed using a sled-track apparatus. The energy absorption characteristic responses of the AA6063-T6 extrusions were compared to experimental results of a commercially available 7xxx series profile. Constitutive modeling and numerical simulations for these AA6063-T6 extrusions were presented and compared with experimental data. Simulations using the Yld2000 anisotropic yield function showed good agreement with the experiments for different crashworthiness parameters.

In the optimization framework, the response surface methodology, coupled with neural network metamodeling and artificial simulated annealing optimization scheme, was used to optimize the size to increase the mean crush force and energy absorption. A new superior UWR4 profile was developed that had a higher mean crush force by 21.9% and 26.7% more energy absorption than the initial size of the UWR4 profile. The specific energy absorption was selected as the optimization objective function. The functionality of the specific energy absorption criteria guided the optimization process to the maximum allowable mass. It was shown that the specific energy absorption linearly relates to the crush efficiency and that the optimization of the specific energy absorption function will tend to simultaneously increase the crush efficiency. An analytical relationship was presented in Equation (27) that relates the specific energy absorption and crush efficiency, and showed good predictive capabilities. Through a sensitivity analysis of the optimization framework, key size sections were identified for critical extrusion process control to manage the mass and efficiency of the energy absorption characteristics of the profile. This framework allows a 6000-series aluminum alloy, in particular AA6063-T6 family alloy, to have competitive energy absorption characteristics compared to mass-produced 7000-series aluminum profiles.

7 Acknowledgements

This work was supported by the Natural Sciences and Engineering Research Council - Automotive Partnership Collaboration (NSERC-APC) and General Motors of Canada. The authors would like to acknowledge Mr. Jeff Wemp at the University of Waterloo for their technical expertise in the

451 crashworthiness experiments. The authors would also like to acknowledge Dr. Jidong Kang and Mr.
452 Waqas Muhammad for performing the tensile tests of the material.

453 **8 References**

- [1] M. Ghanna, M. Niesluchowski and P. Culkeen, "Analysis of a Frontal Rail Structure in a Frontal Collision," in *SAE 2002 World Congress*, Detroit, Michigan, 2002.
- [2] W. Abramowicz, "The Effective Crushing Distance in Axially Compressed Thin-Walled Metal Columns," *International Journal of Impact Engineering*, vol. 1, no. 3, pp. 309-317, 1983.
- [3] W. Abramowicz and N. Jones, "Dynamic Axial Crushing of Circular Tubes," *International Journal of Impact Engineering*, vol. 2, no. 3, pp. 263-281, 1984.
- [4] W. Abramowicz and N. Jones, "Dynamic Axial Crushing of Square Tubes," *International Journal of Impact Engineering*, vol. 2, no. 2, pp. 79-208, 1984.
- [5] W. Abramowicz and N. Jones, "Dynamic Progressive Buckling of Circular and Square Tubes," *International Journal of Impact Engineering*, vol. 4, no. 4, pp. 243-270, 1986.
- [6] W. Abramowicz and T. Wierzbicki, "Axial Crushing of Multicorner Sheet Metal Columns," *Journal of Applied Mechanics*, vol. 56, no. March, pp. 113-120, 1989.
- [7] N. Jones and T. Wierzbicki, *Structural Crashworthiness*, London: Butterworths, 1983.
- [8] N. Jones, *Structural Impact - 2nd Edition*, New York, NY, USA: Cambridge University Press, 2012.
- [9] T. Wierzbicki, "Crushing Analysis of Metal Honeycombs," *International Journal of Impact Engineering*, vol. 1, no. 2, pp. 157-174, 1983.
- [10] T. Wierzbicki and W. Abramowicz, "On the Crushing Mechanics of ThinWalled Structures," *Journal of Applied Mechanics*, vol. 50, no. December, pp. 727-734, 1983.
- [11] N. Jones and T. Wierzbicki, *Structural Crashworthiness and Failure*, New York: Elsevier Applied Science, 1993.
- [12] M. Langseth, O. Hopperstad and T. Berstad, "Crashworthiness of Aluminum Extrusions: Validation of Numerical Simulation, Effect of Mass Ratio and Impact Velocity," *International Journal of Impact Engineering*, pp. 829-854, 1999.
- [13] M. Langseth and O. Hopperstad, "Static and Dynamic Axial Crushing of Square Thin-Walled Aluminum Extrusions," *International Journal of Impact Engineering*, vol. 18, no. 7-8, pp. 949-968, 1996.

- [14] H.-S. Kim, "New extruded multi-cell aluminum profile for maximum crash energy absorption and weight efficiency," *Thin-Walled Structures*, vol. 40, pp. 311-327, 2002.
- [15] R. Mayer, B. Peterson, R. Mishra and A. Sachdev, "The Effect of Tempering (Artificial Aging) On the Crashworthiness Performance of Mass-Efficient Extruded Aluminum Structures," in *ASME 2003 Design Engineering Technical Conferences and Computers and Information in Engineering Conference*, Chicago, Illinois, USA, 2003.
- [16] K. Yamazaki and J. Han, "Maximization of the crushing energy absorption of tubes," *Structural Optimization*, vol. 16, pp. 37-46, 1998.
- [17] K. Yamazaki and J. Han, "Maximization of the crushing energy absorption of cylindrical shells," *Advances in Engineering Software*, vol. 31, pp. 425-434, 2000.
- [18] H. Zarei and M. Kroger, "Multiobjective crashworthiness optimization of circular aluminum tubes," *Thin-Walled Structures*, vol. 44, pp. 301-308, 2006.
- [19] J. Marzbanrad and M. Ebrahimi, "Multi-Objective Optimization of aluminum hollow tubes for vehicle crash energy absorption using a genetic algorithm and neural networks," *Thin-Walled Structures*, vol. 49, pp. 1605-1615, 2011.
- [20] J. Forsberg and L. Nilsson, "On Polynomial Response Surfaces and Kriging for Use in Structural Optimization of Crashworthiness," *Journal of Structural Multidisciplinary Optimization*, vol. 29, pp. 232-243, 2005.
- [21] Y. Liu, "Optimum Design of Straight Thin-Walled Box Section Beams for Crashworthiness Analysis," *Finite Elements in Analysis and Design*, vol. 44, pp. 139-147, 2008.
- [22] T. Jansson, L. Nilsson and M. Redhe, "Using surrogate models and response surfaces in structural optimization - with application to crashworthiness design and sheet metal forming," *Structural Multidisciplinary Optimization*, vol. 25, pp. 129-140, 2003.
- [23] S. Yang and C. Qi, "Multiobjective optimization for empty and foam-filled square columns under oblique impact loading," *International Journal of Impact Engineering*, vol. 54, pp. 177-191, 2013.
- [24] W. Roux, N. Stander and R. Haftka, "Response surface approximations for structural optimization," *International Journal for Numerical Methods in Engineering*, vol. 42, pp. 517-534, 1998.
- [25] S. Esfahlani, H. Shirvani, A. Shirvani, S. Nwaubani, H. Mebrahtu and C. Chriwa, "Hexagonal honeycomb cell optimisation by way of meta-model techniques," *International Journal of Crashworthiness*, vol. 18, no. 3, pp. 264-275, 2013.
- [26] C. Kohar, M. Mohammadi, R. Mishra and K. Inal, "Effects of elastic-plastic behaviour on the axial crush response of square tubes," *Thin-Walled Structures*, vol. 93, pp. 64-87, 2015.
- [27] J. Hallquist, LS-DYNA Theory Manual, Livermore, California: Livermore Software Technology Corporation, 2006.

- [28] S. Hsu and N. Jones, "Quasi-static and Dynamic Axial Crushing of Thin-Walled Circular Stainless Steel, Mild Steel and Aluminum Alloy Tubes," *International Journal of Crashworthiness*, vol. 9, no. 2, pp. 195-217, 2004.
- [29] A. Bardelcik, M. Worswick and M. Wells, "The influence of martensite, bainite and ferrite on the as-quenched constitutive response of simultaneously quenched and deformed boron steel - Experiments and model," *Materials and Design*, vol. 55, pp. 509-525, 2014.
- [30] G. Cowper and P. Symonds, "Strain Hardening and Strain-Rate Effects in the Impact Loading of Centilevered Beams," Brown University Division of Applied Mathematics, Providence, Rhode Island, USA, 1957.
- [31] B. Williams, C. Simha, N. Aberdrabbo, R. Mayer and M. Worswick, "Effect of anisotropy, kinematic hardening, and strain-rate sensitivity on the predicted axial crush of hydroformed aluminum alloy tubes," *International Journal of Impact Engineering*, vol. 37, pp. 652-661, 2010.
- [32] A. Hanssen, M. Langseth and O. Hopperstad, "Static and Dynamic Crushing of Square Aluminum Extrusions with Aluminum Foam Filler," *International Journal of Impact Engineering*, vol. 24, pp. 347-383, 2000.
- [33] C. Kohar, M. Mohammadi, R. Mishra and K. Inal, "The effects of anisotropic yield functions on the axial crush response of circular crush tubes," *Thin-Walled Structures*, p. Submitted, 2016.
- [34] B. Plunkett, O. Cazacu and F. Barlat, "Orthotropic yield criteria for description of the anisotropy in tension and compression of sheet metals," *International Journal of Plasticity*, vol. 24, pp. 847-866, 2008.
- [35] F. Barlat and J. Lian, "Plastic behaviour and stretchability of sheet metals. Part I: A yield function for orthotropic sheets under plane stress conditions," *International Journal of Plasticity*, vol. 5, pp. 51-66, 1989.
- [36] M. Jansson, L. Nilsson and K. Simonsson, "On strain localisation in tube hydroforming of aluminium extrusions," *Journal of Materials Processing Technology*, vol. 195, pp. 3-14, 2008.
- [37] D. Achani, O. Hopperstad and O.-G. Lademo, "Behaviour of extruded aluminum alloys under proportional and non-proportional strain paths," *Journal of Materials Processing Technology*, vol. 209, pp. 4750-4764, 2009.
- [38] F. Barlat, J. Brem, J. Yoon, K. Chung, R. Dick, D. Lege, F. Pourboghrat, S.-H. Choi and E. Chu, "Plane stress yield function for aluminum alloy sheets - part 1: theory," *International Journal of Plasticity*, vol. 19, pp. 1297-1319, 2003.
- [39] F. Barlat, H. Aretz, J. Yoon, M. Karabin, J. Brem and R. Dick, "Linear transformation-based anisotropic yield functions," *International Journal of Plasticity*, vol. 21, pp. 1009-1039, 2005.
- [40] W. Hosford, "On the crystallographic basis of yield criteria," *Textures and Microstructures*, Vols. 26-27, pp. 479-493, 1996.

- [41] D. Ghaffari Tari, M. Worswick, U. Ali and M. Gharghoui, "Mechanical response of AZ31B magnesium alloy: Experimental characterization and material modeling considering proportional loading at room temperature," *International Journal of Plasticity*, pp. 247-267, 2014.
- [42] N. Norton, *Design of machinery: an introduction to the synthesis and analysis of mechanisms and machines*, New York: McGraw-Hill, 2004.
- [43] E. Avallone, T. Baumeister and A. Sadegh, *Mark's Standard Handbook for Mechanical Engineers*, New York: McGraw-Hill, 2007.
- [44] W. Abramowicz, "The Macro Element Approach in Crash Calculations, in: Ambrosio, J.C.C, Pereira, M.F.O.S, da Silva, F.P.," in *Crashworthiness of Transportation Systems: Structural Impact and Occupant Protection*, vol. 332, Dordrecht, Kluwer Academic Publishers, 1997, pp. 291-320.
- [45] N. Stander, W. Roux, M. Giger, M. Redhe, N. Fedorova and J. Haarhoff, "Crashworthiness Optimization in LS-OPT: Case Studies in Metamodeling and Random Search Techniques," *4th European LS-DYNA Users Conferece*, pp. J-I-11-26, 2003.
- [46] M. Papadrakakis, N. Lagaros and Y. Tsompanakis, "Strucutral optimization using evolution strategies and neural networks," *Computer Methods in Applied Mechanics and Engineering*, vol. 156, pp. 309-333, 1998.
- [47] K. Hornik, M. Stinchombe and W. Halbert, "Universal Appoximation of an Unknown Mapping and Its Derivatives Using Multilayer Feedforward Networks," *Neural Networks*, vol. 3, pp. 551-560, 1990.
- [48] V. Cerny, "Thermodynamical Approach to the Traveling Salesman Problem: An Efficient Simulation Algorithm," *Journal of Optimization Theory and Applications*, vol. 45, no. 1, pp. 41-51, 1985.
- [49] M. Pincus, "A Monte Carlo Method for the Approximate Solution of Certian Types of Constrained Optimization Problems," *Operations Research*, vol. 18, pp. 1225-1228, 1970.
- [50] S. Kirkpatrick, C. Gelatt and M. Vecchi, "Optimization by Simulated Annealing," *Science*, vol. 220, no. 4598, pp. 671-680, 1983.
- [51] N. Stander and K. Craig, "On the robustness of a simple domain reduction scheme for simulation-based optimization," *Engineering Computations*, vol. 19, no. 4, pp. 431-450, 2002.

454

455

456

457 **APPENDIX**

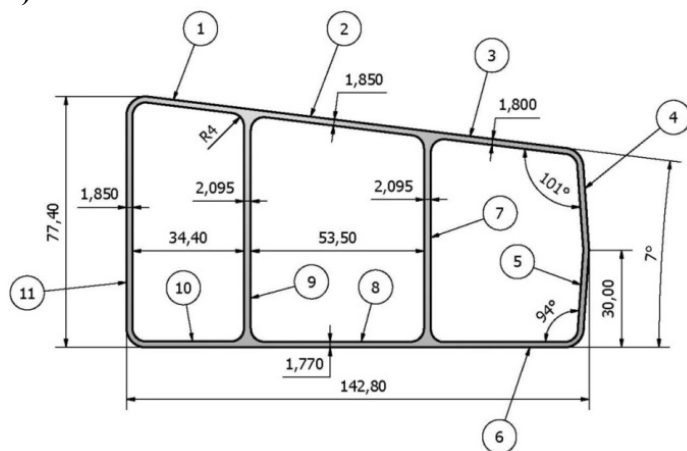
458 *A.1 – Numerical Simulation Parameter Test Matrix*

Input Parameters: Wall Thickness						Output Response: Energy Absorption Characteristics						
#	t ₁ [mm]	t ₂ [mm]	t ₃ [mm]	t ₄ [mm]	t ₅ [mm]	Mass [kg]	F _{mean} [kN]	F _{peak} [kN]	Eff. η	Meas. SEA [kJ/kg]	Pred. SEA [kJ/kg]	Residual Error [%]
1	1.82	1.85	2.09	1.80	1.88	1.278	116.74	218.41	0.53	91.367	91.204	0.179
2	1.75	2.40	1.75	2.08	2.40	1.383	132.37	239.62	0.55	95.707	95.548	0.166
3	2.40	2.40	2.40	2.24	2.24	1.574	164.18	284.80	0.58	104.326	104.268	0.056
4	2.08	1.75	2.40	1.75	2.40	1.385	134.59	238.31	0.56	97.176	98.910	-1.784
5	2.40	2.32	2.32	2.40	1.75	1.523	156.56	278.40	0.56	102.825	102.838	-0.012
6	1.83	2.32	1.75	1.91	1.75	1.296	118.32	221.94	0.53	91.295	91.293	0.003
7	1.91	1.75	2.24	2.40	1.75	1.366	132.42	244.08	0.54	96.941	96.928	0.014
8	1.75	2.40	2.40	1.75	2.24	1.443	141.20	247.54	0.57	97.833	97.459	0.382
9	2.40	1.75	1.75	1.75	2.24	1.284	118.03	217.30	0.54	91.956	95.233	-3.563
10	1.75	1.75	2.08	2.40	2.32	1.373	134.56	242.06	0.56	98.019	98.509	-0.499
11	2.32	1.75	2.39	2.40	2.40	1.494	153.88	270.89	0.57	103.007	102.051	0.928
12	2.14	1.97	1.75	2.35	2.39	1.387	137.14	246.64	0.56	98.871	101.334	-2.491
13	2.00	2.19	2.14	2.39	2.10	1.459	147.88	262.12	0.56	101.353	101.672	-0.314
14	1.87	1.82	1.84	1.83	2.39	1.283	120.54	218.62	0.55	93.967	93.685	0.300
15	1.94	2.36	2.28	2.02	1.75	1.425	139.31	251.06	0.55	97.760	97.368	0.401
16	2.24	2.32	1.75	2.00	2.16	1.386	136.75	240.27	0.57	98.633	98.447	0.189
17	1.78	1.76	1.75	2.22	1.90	1.255	113.50	219.01	0.52	90.455	90.601	-0.162
18	2.27	2.32	2.24	1.75	2.12	1.442	141.78	248.43	0.57	98.316	98.840	-0.533
19	2.30	1.76	2.40	1.75	1.76	1.350	130.28	232.59	0.56	96.500	96.991	-0.509
20	2.39	1.91	2.13	2.09	2.07	1.408	140.21	249.08	0.56	99.591	99.204	0.388
21	2.16	1.96	2.37	2.40	2.24	1.494	152.16	270.86	0.56	101.862	102.933	-1.052
22	2.24	2.08	2.04	2.26	2.26	1.444	145.81	258.03	0.57	100.966	101.061	-0.094
23	2.25	1.85	2.00	2.06	2.31	1.378	136.01	241.76	0.56	98.683	98.651	0.032
24	2.23	2.12	2.14	2.26	1.89	1.434	144.81	257.43	0.56	100.974	100.160	0.806
25	2.01	2.10	2.25	2.01	2.40	1.442	147.09	253.30	0.58	101.988	101.979	0.008
26	2.01	1.83	2.07	2.26	2.29	1.389	137.56	246.87	0.56	99.059	99.698	-0.645
27	2.40	1.91	2.30	2.38	2.02	1.474	150.69	267.96	0.56	102.228	101.510	0.702
28	2.02	2.07	2.31	2.07	2.11	1.431	142.68	253.24	0.56	99.720	100.857	-1.140
29	2.10	1.76	2.17	2.31	2.00	1.385	136.12	248.13	0.55	98.302	99.076	-0.787
30	2.28	1.94	2.40	2.12	2.14	1.462	149.29	261.41	0.57	102.145	102.193	-0.047
31	2.21	2.10	2.24	2.26	2.40	1.494	156.04	268.38	0.58	104.457	103.849	0.581
32	2.20	2.28	2.19	2.07	2.12	1.462	146.75	258.74	0.57	100.371	100.243	0.128
33	2.30	2.20	2.17	2.38	2.11	1.496	151.48	270.92	0.56	101.272	101.885	-0.605
34	2.16	1.96	2.21	2.09	2.27	1.426	143.77	252.37	0.57	100.828	100.652	0.175
35	2.37	1.90	2.22	2.30	2.32	1.472	149.12	265.11	0.56	101.333	101.587	-0.250
36	2.28	1.93	2.07	2.34	2.07	1.423	141.28	255.85	0.55	99.316	99.753	-0.440
37	2.09	2.07	2.06	2.13	2.08	1.397	137.97	246.97	0.56	98.735	98.190	0.553
38	2.38	2.11	2.40	2.32	2.24	1.535	160.08	278.88	0.57	104.281	103.707	0.551
39	1.98	2.16	2.26	2.28	2.30	1.478	153.21	264.40	0.58	103.680	103.186	0.477
40	2.18	2.32	2.12	2.11	2.39	1.484	154.01	262.68	0.59	103.795	102.812	0.948
41	1.95	2.16	2.30	2.30	2.40	1.494	156.08	267.43	0.58	104.478	103.897	0.557
42	1.85	2.27	2.09	2.38	2.37	1.471	148.60	262.26	0.57	100.999	101.495	-0.491
43	2.07	2.01	2.12	2.40	2.25	1.448	146.81	260.43	0.56	101.376	102.094	-0.709

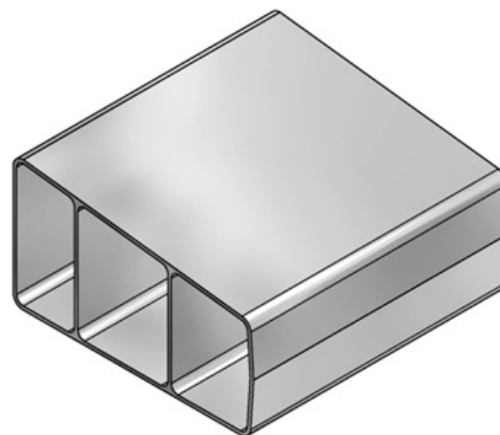
44	1.97	2.31	2.29	2.13	2.04	1.463	147.95	259.86	0.57	101.136	101.386	-0.247
45	2.12	2.30	2.36	2.36	2.12	1.527	159.55	276.77	0.58	104.478	103.849	0.603
46	1.98	2.24	2.40	2.08	2.26	1.486	153.54	263.66	0.58	103.322	103.479	-0.152
47	1.75	2.01	2.22	2.28	2.19	1.413	142.10	249.64	0.57	100.575	100.206	0.366
48	1.91	2.19	2.05	2.17	2.19	1.413	139.16	249.28	0.56	98.517	98.819	-0.307
49	2.02	1.92	2.34	2.27	2.39	1.464	152.27	262.26	0.58	103.996	103.582	0.398
50	1.92	2.01	2.39	2.37	2.19	1.473	151.94	264.40	0.57	103.148	102.964	0.179
51	1.94	2.07	2.40	2.28	2.40	1.494	155.62	267.49	0.58	104.178	104.253	-0.071
52	2.13	2.34	2.07	2.38	2.29	1.500	151.41	270.07	0.56	100.953	101.598	-0.638
53	1.77	1.89	2.40	2.37	2.36	1.456	150.78	258.82	0.58	103.568	102.549	0.983
54	1.98	2.12	2.39	2.27	1.98	1.464	148.96	262.95	0.57	101.717	102.071	-0.349
55	1.86	1.96	2.16	2.37	2.39	1.435	147.19	255.51	0.58	102.564	102.322	0.236
56	1.92	1.89	2.19	2.06	2.30	1.386	138.16	243.24	0.57	99.714	99.208	0.507
57	1.98	1.94	2.20	2.25	2.11	1.410	143.45	251.32	0.57	101.772	100.327	1.420
58	1.76	2.03	1.96	2.39	2.20	1.385	134.23	244.71	0.55	96.902	97.643	-0.765
59	1.88	1.84	2.40	2.18	2.23	1.421	144.48	252.25	0.57	101.641	100.642	0.983
60	1.75	2.20	2.33	2.15	2.20	1.448	147.69	255.16	0.58	102.023	101.052	0.952
61	1.93	2.04	2.40	2.32	2.40	1.493	156.03	267.66	0.58	104.488	104.224	0.253
62	2.04	2.06	2.27	2.18	2.39	1.464	150.46	260.86	0.58	102.763	103.204	-0.429
63	2.13	2.19	2.17	2.33	2.22	1.481	154.50	266.48	0.58	104.352	102.510	1.764
64	1.89	2.08	2.39	2.15	2.28	1.460	149.01	259.17	0.57	102.037	102.982	-0.926
65	1.77	1.97	2.39	2.21	2.33	1.443	147.01	255.12	0.58	101.885	102.169	-0.278
66	2.10	1.91	2.21	2.28	2.27	1.437	148.20	257.50	0.58	103.126	102.319	0.783
67	1.76	2.19	2.21	2.31	2.26	1.452	146.92	257.38	0.57	101.196	101.735	-0.533
68	2.05	1.97	2.32	2.17	2.22	1.443	147.58	257.35	0.57	102.287	102.620	-0.325
69	1.87	2.06	2.14	2.37	2.23	1.434	145.30	255.68	0.57	101.315	101.625	-0.306
70	1.87	2.25	2.23	2.05	2.35	1.450	144.53	254.46	0.57	99.684	100.057	-0.374

460 **List of Figures**

a)

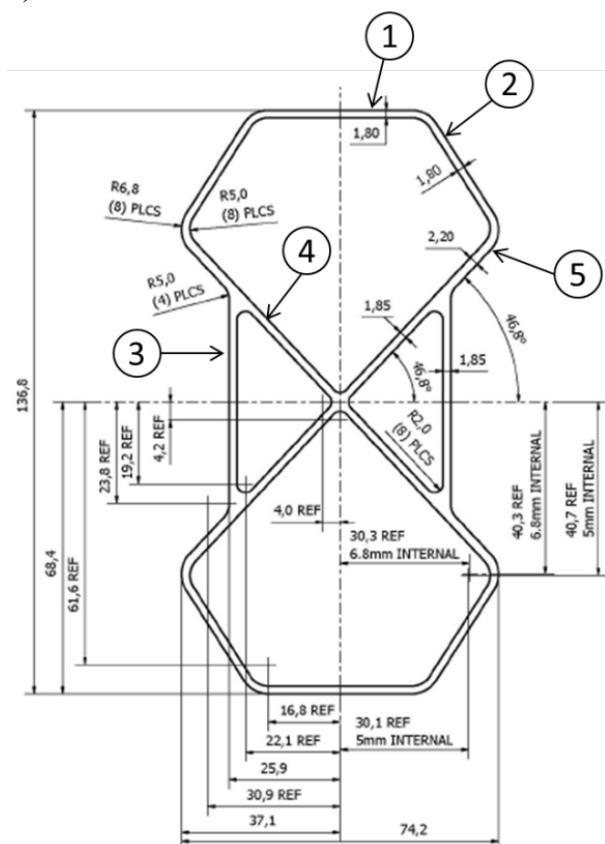


b)

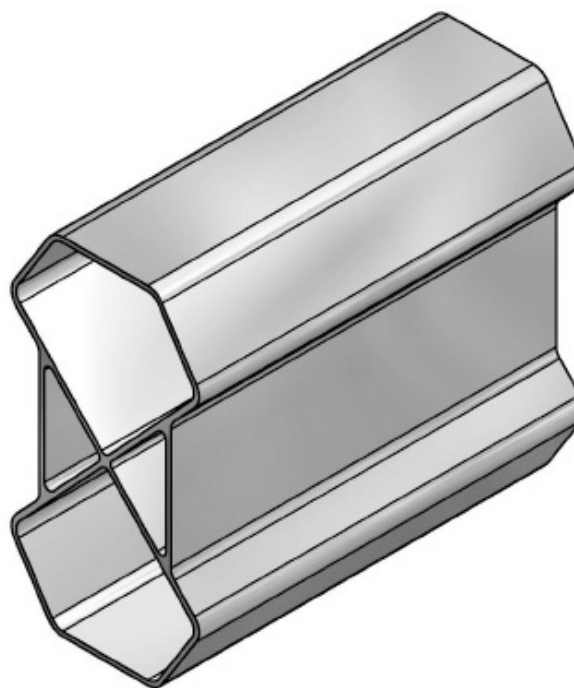


461 **Figure 1 – (a) Cross Section and (b) Isometric view of baseline extrusion profile**

b)



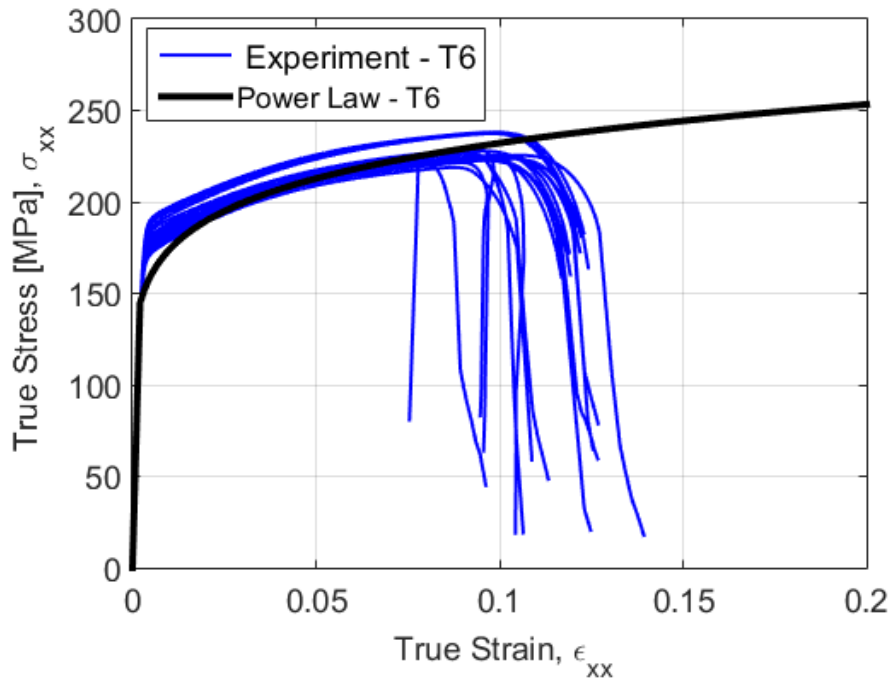
b)



462 **Figure 2 – (a) Cross Section and (b) Isometric view of new UW-R4 extrusion profile**

463

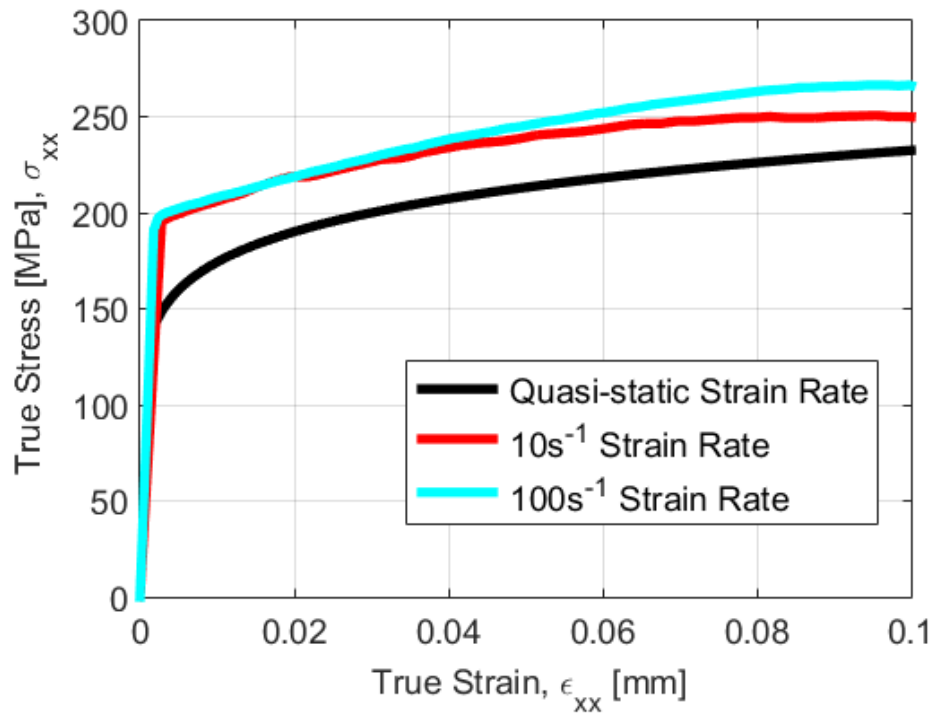
464



465

466

Figure 3 – Stress-strain from tensile tests of extrusion AA6063-T6 for various locations at quasi-static strain rate



467

468

Figure 4 – Stress-strain response for quasi-static, 10 s⁻¹, 100 s⁻¹ strain rates of extrusion AA6063-T6

469

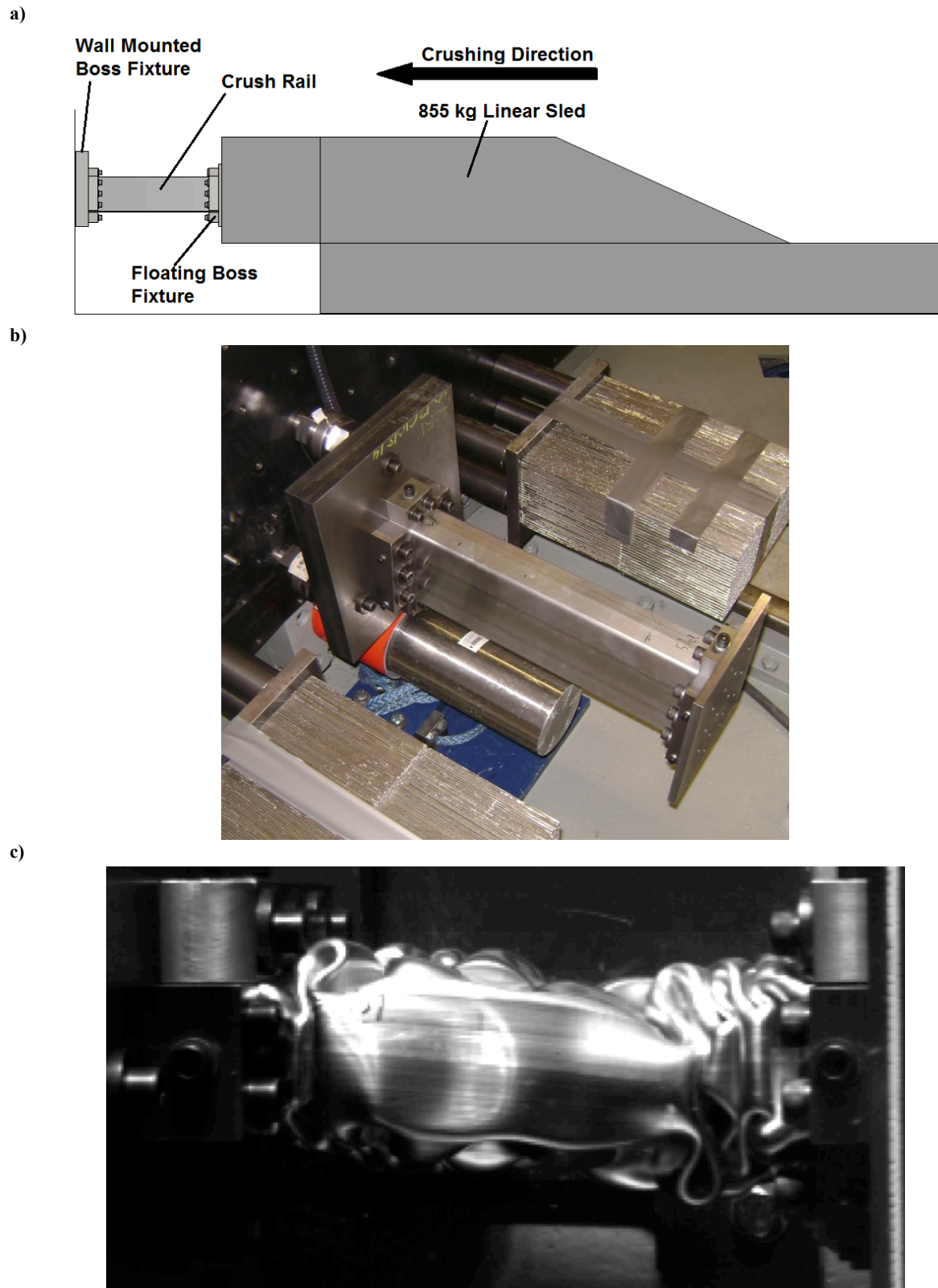


Figure 5 – (a) Schematic of the sled-track testing apparatus, (b) experimental setup and (c) tube crushing during impact

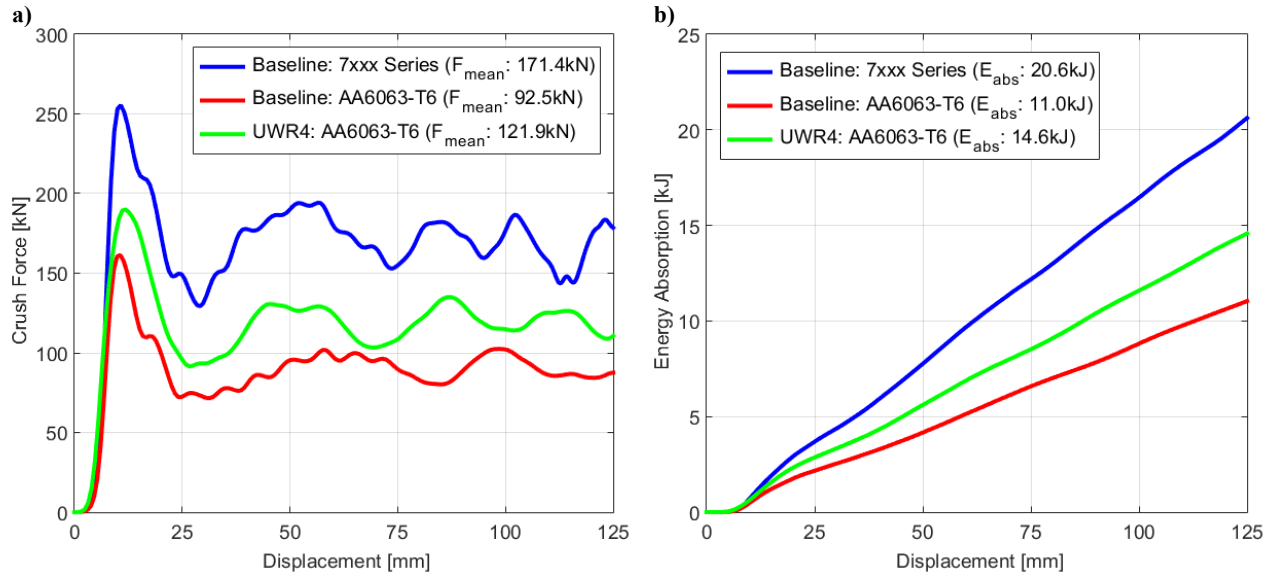


Figure 6 – Experimental (a) force-displacement and (b) energy response for Baseline Profile – 7xxx Series, Baseline Profile – AA6063-T6 and UWR4 Profile – AA6063-T6

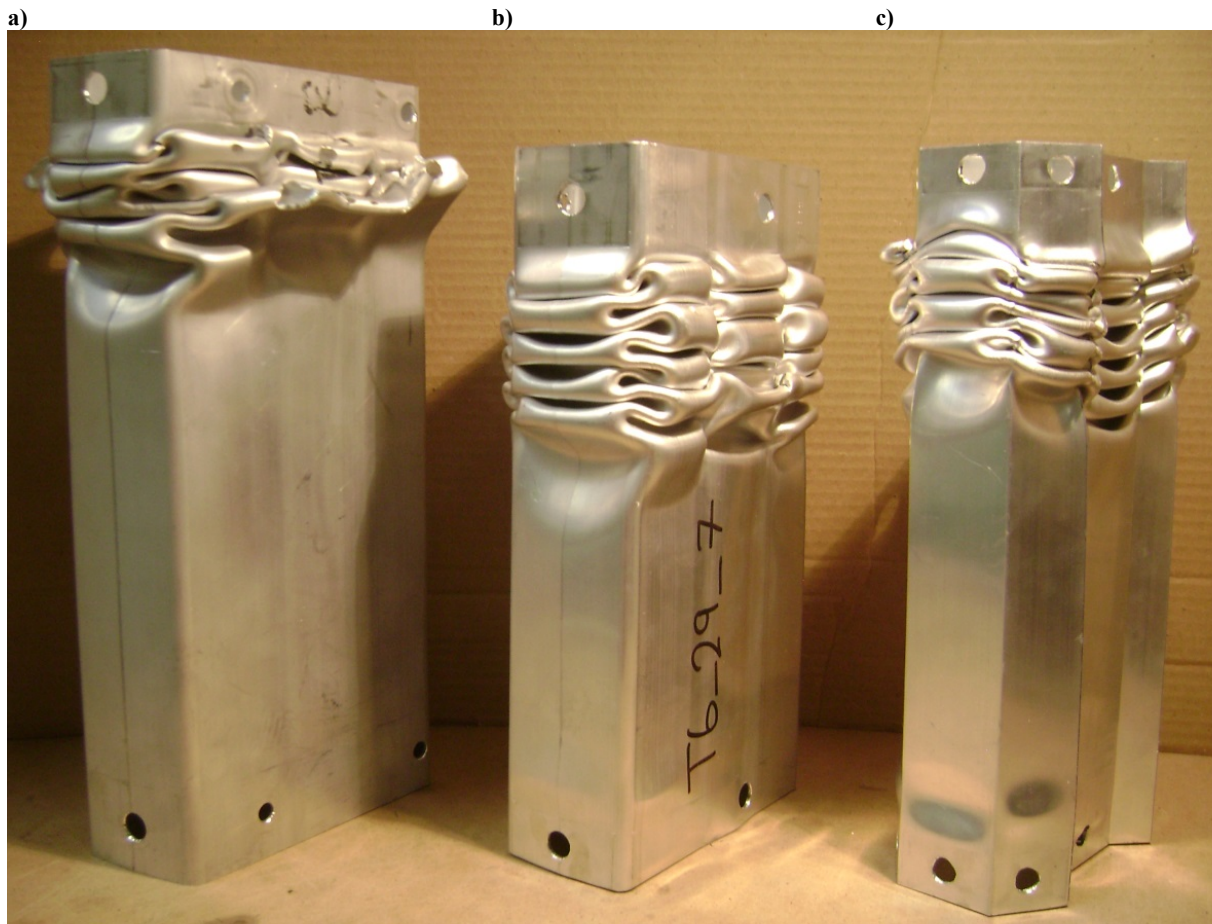


Figure 7 – Experimentally crushed (a) Baseline Profile – 7xxx Series, (b) Baseline Profile – AA6063-T6, and (c) UWR4 Profile – AA6063-T6

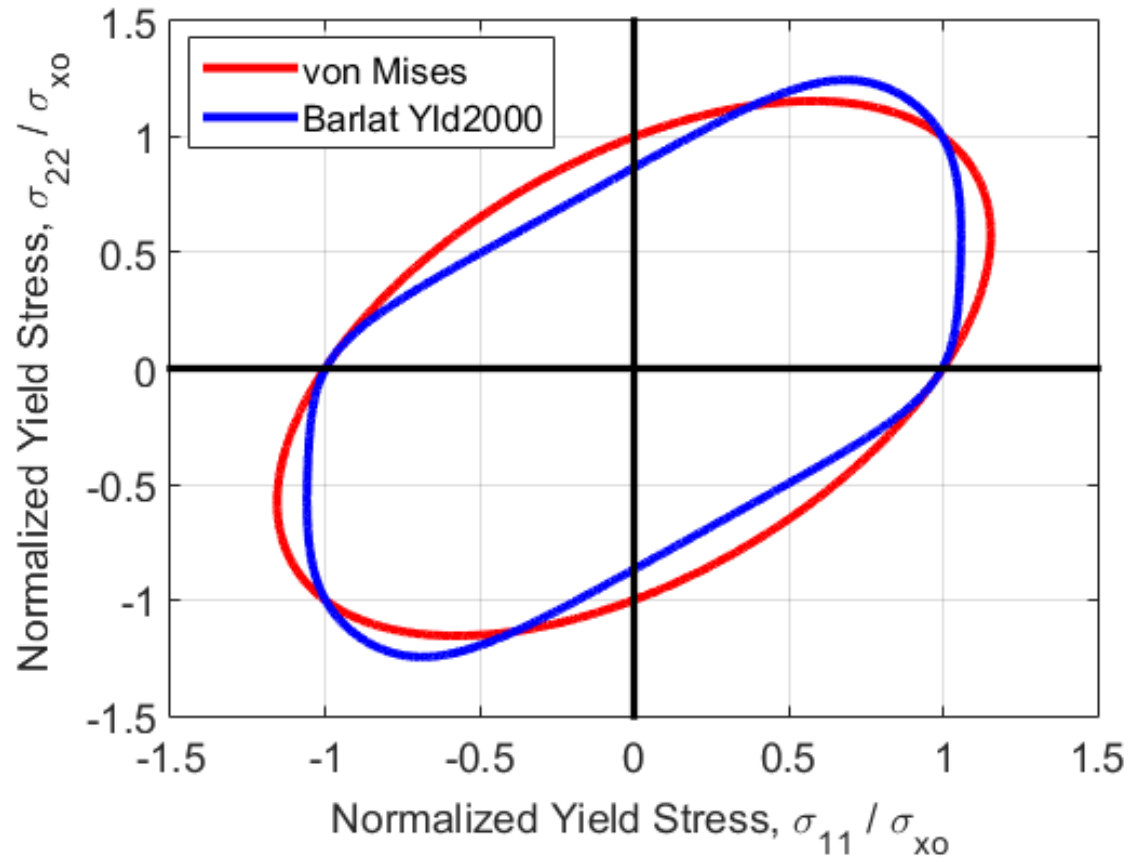
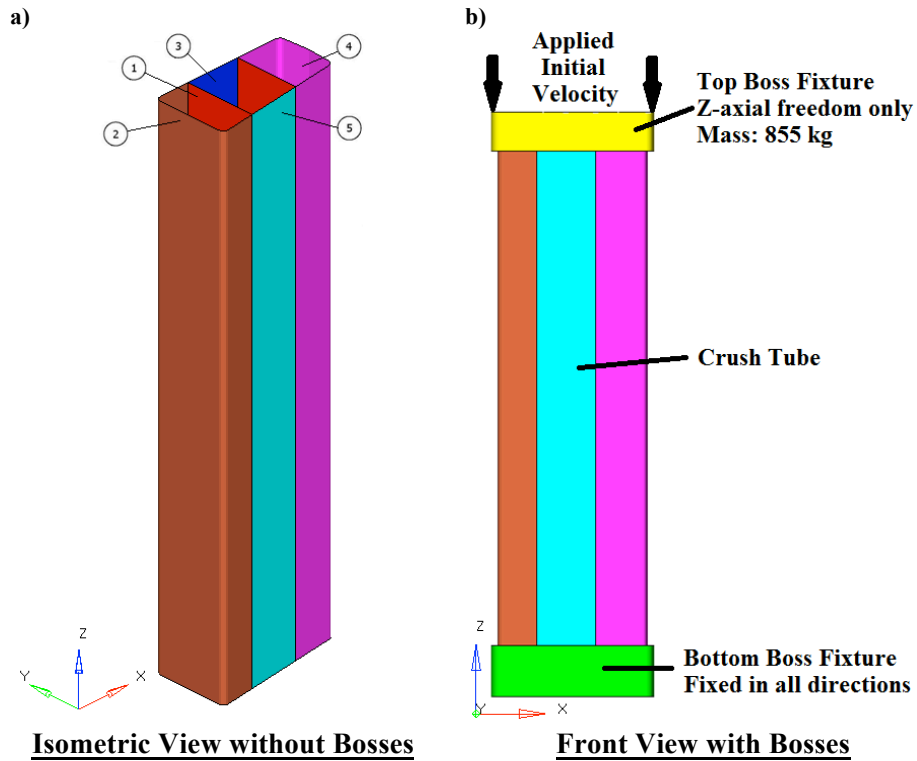
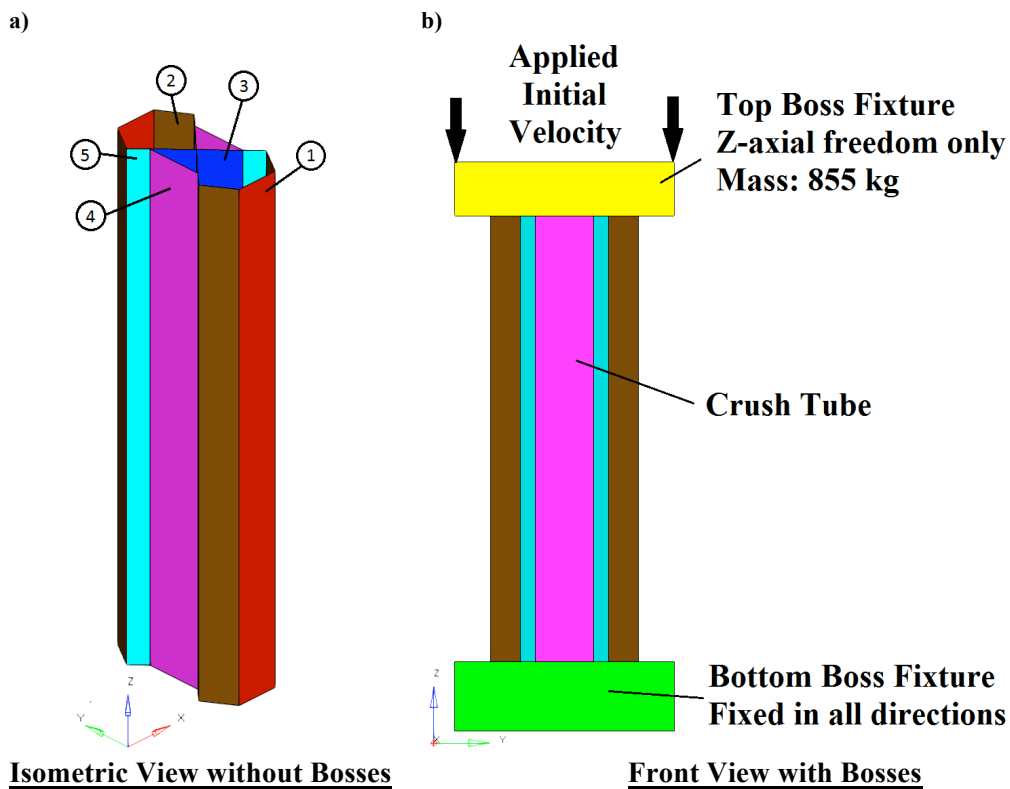


Figure 8 - Yield surface shape for the isotropic von Mises and anisotropic Barlat *et al* Yld2000

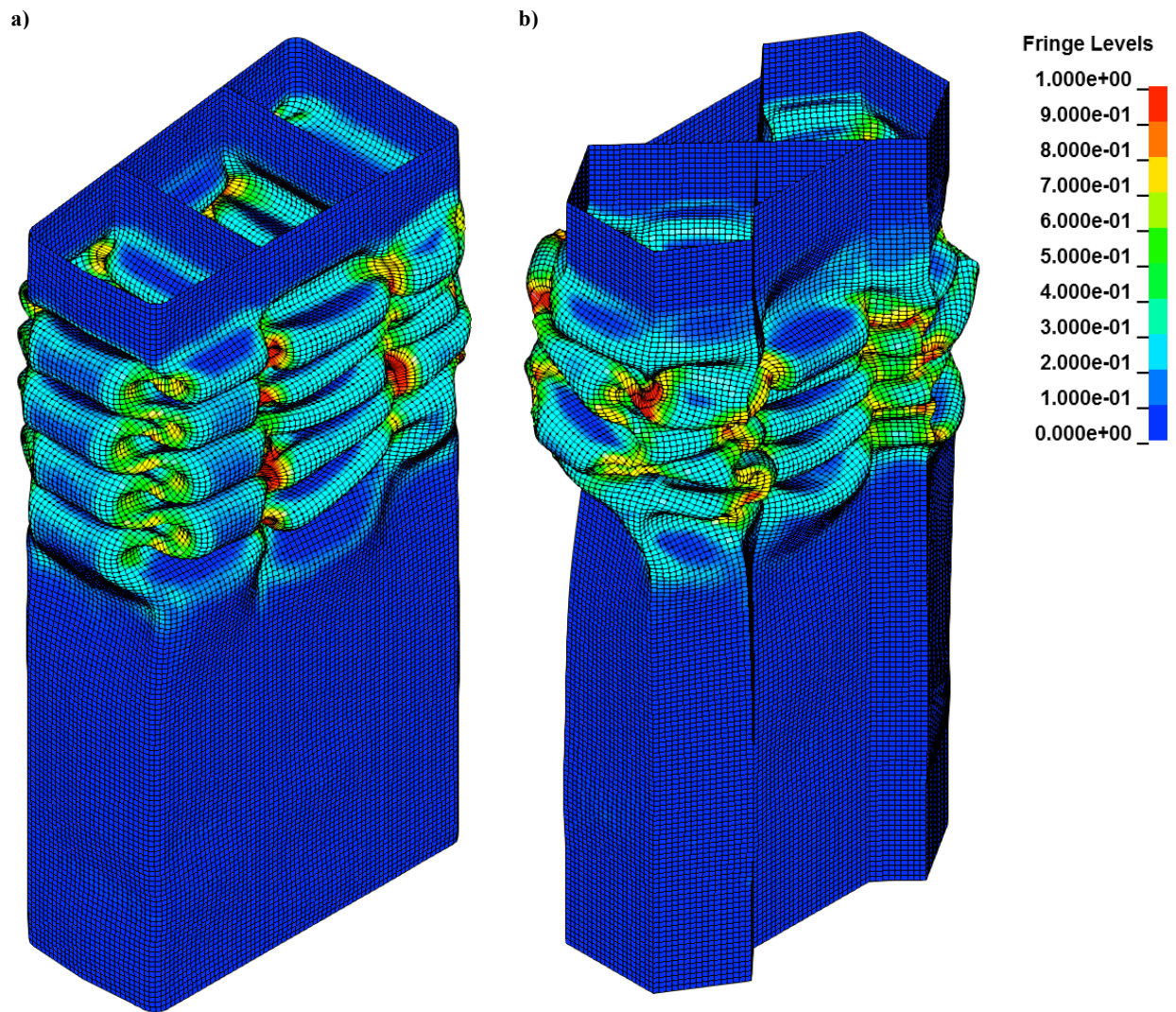


481 **Figure 9** – (a) Isometric View without Bosses and (b) Front View with Bosses of Omega Profile



482 **Figure 10** – (a) Isometric View without Bosses and (b) Front View with Bosses of UWR4 Profile

483



484 **Figure 11** – Simulated crush tube effective strain contours for (a) Baseline Profile – AA6063-T6, and (b) UWR4 Profile –
485 AA6063-T6 models

486

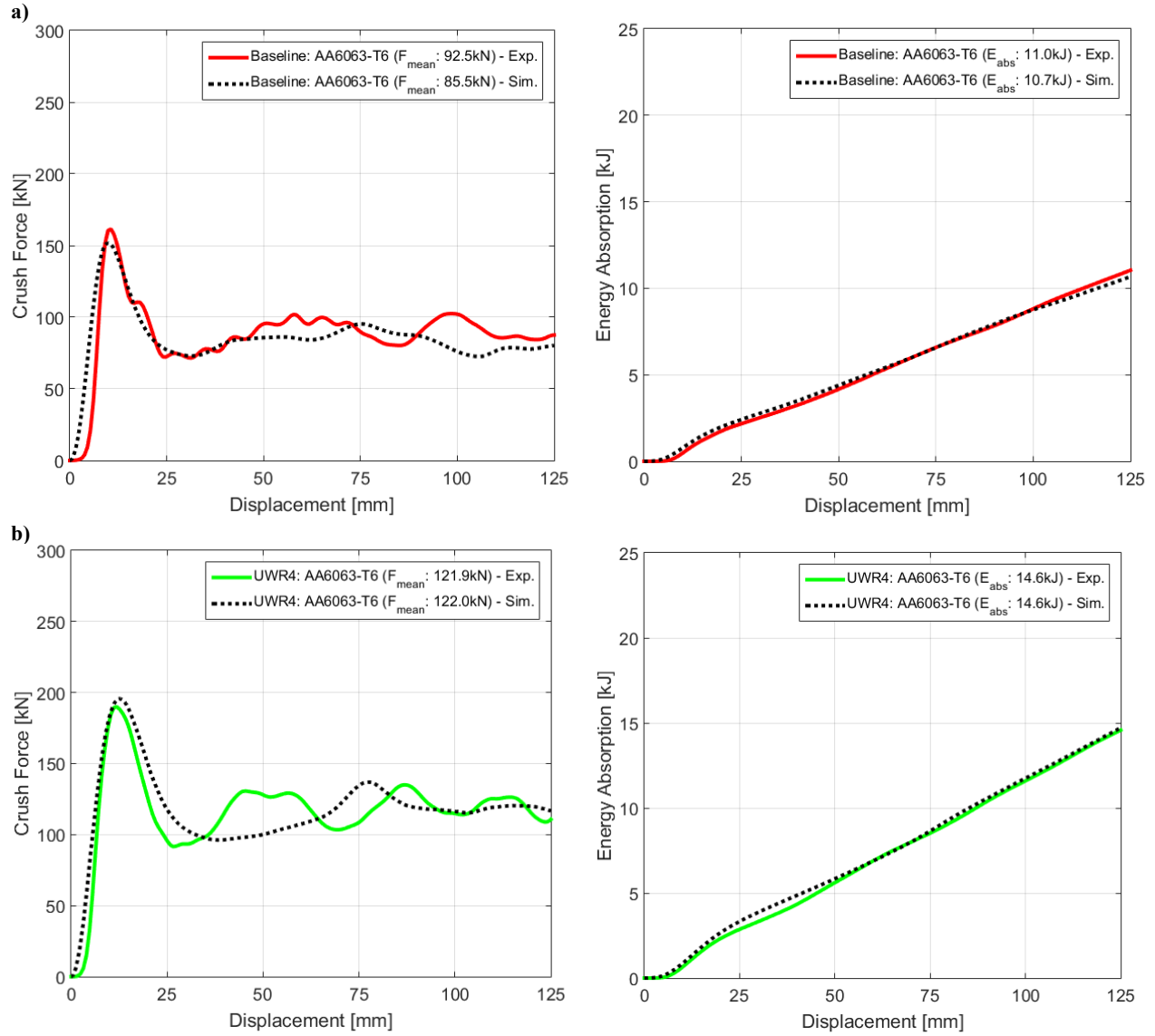


Figure 12 – Comparison of simulation and experimental force-displacement and energy absorption response for (a) Baseline Profile - AA6063-T6 and (b) UWR4 Profile - AA6063-T6

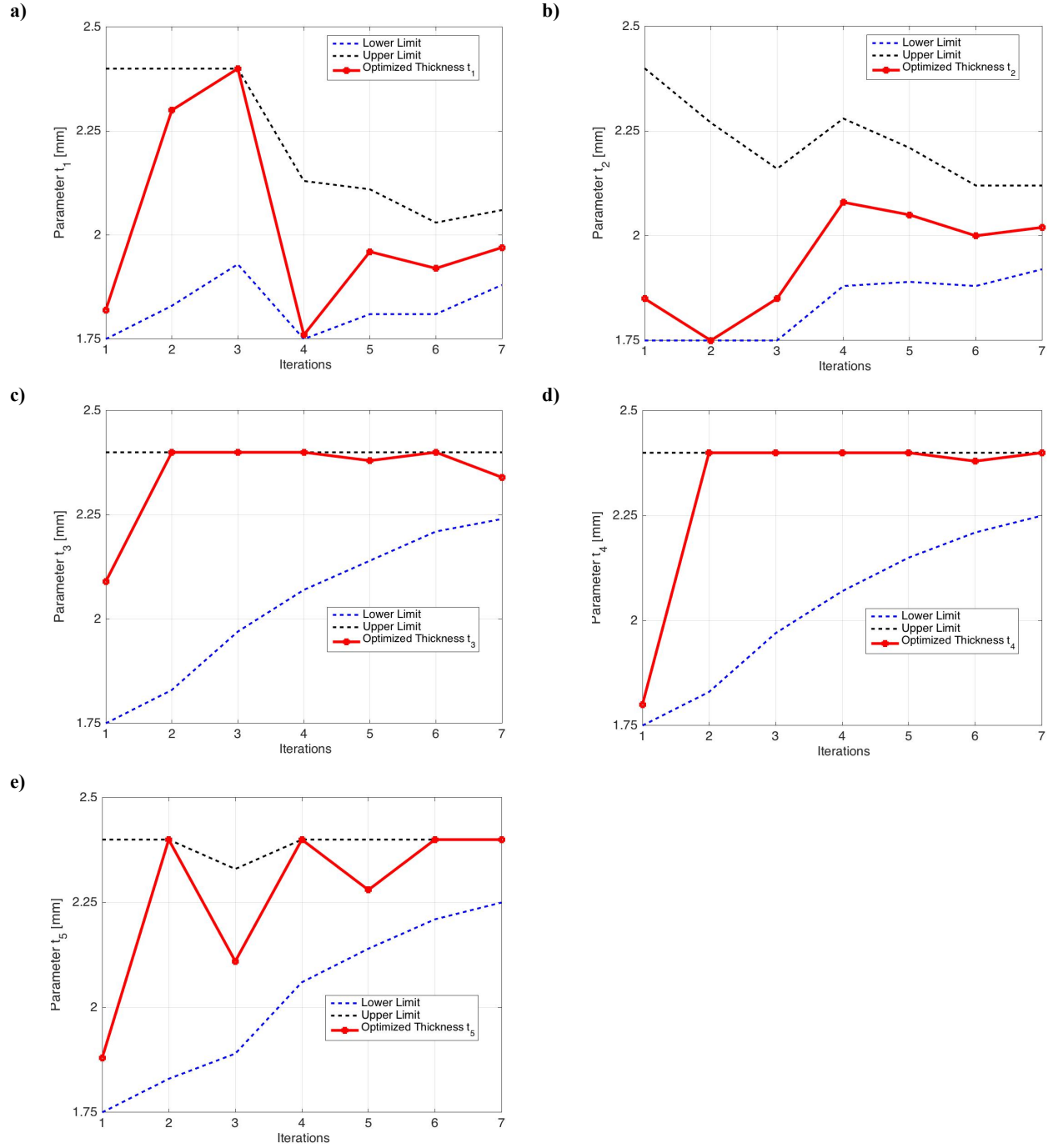
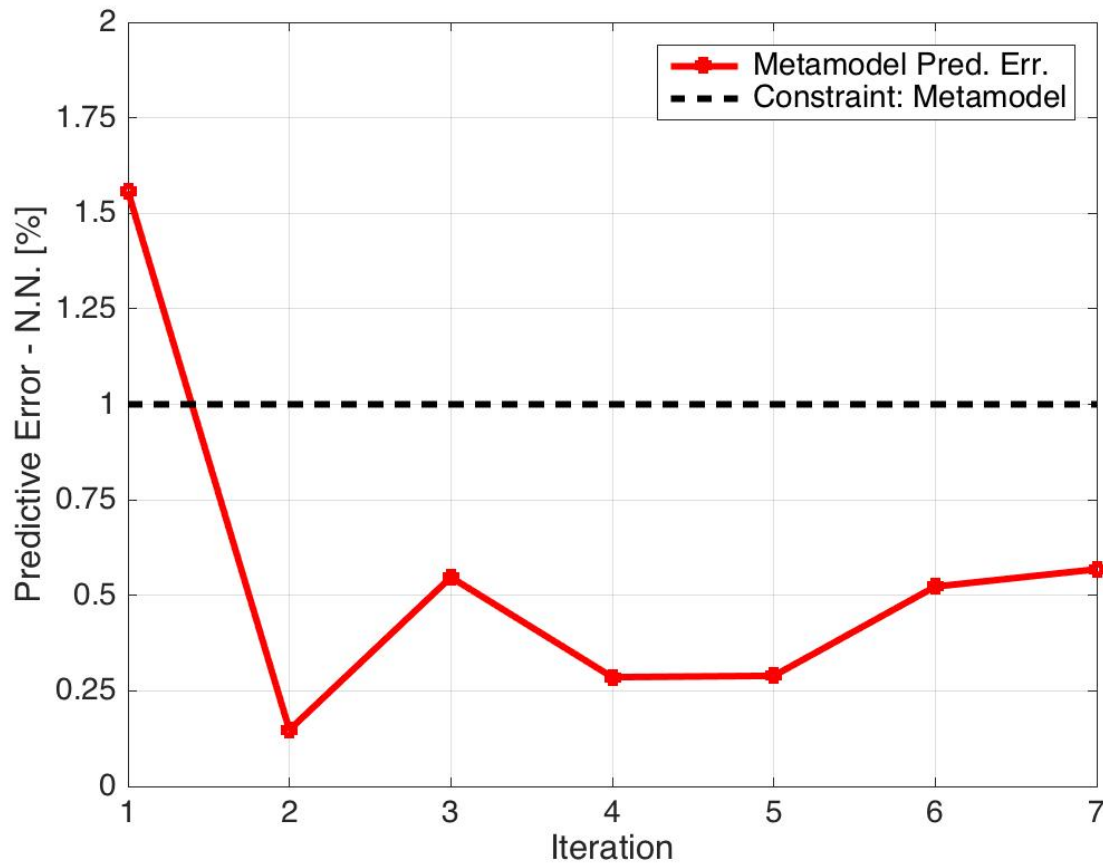


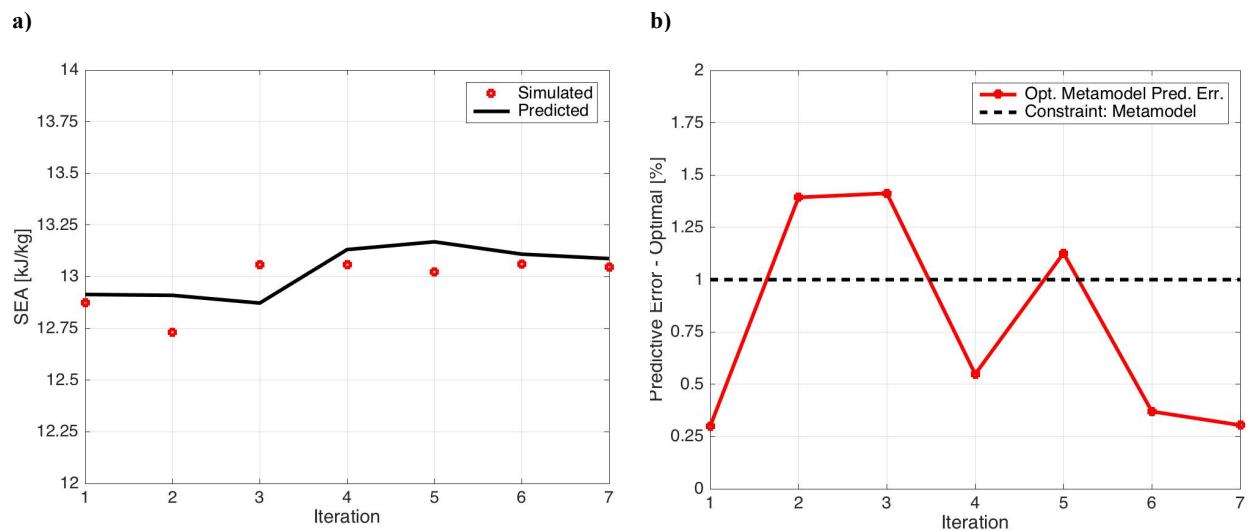
Figure 13 – Parameter Convergence Plot of Crush Rail Wall Thickness Parameters (a) t_1 , (b) t_2 , (c) t_3 , (d) t_4 and (e) t_5 using Isotropic Material Model (UWR4)

496



497

498 **Figure 14** – Convergence Plot of Metamodel Prediction Error of Specific Energy Absorption using Isotropic Material Model
 499 (UWR4)



500 **Figure 15** – Convergence Plot of a) Predicted and Simulated b) Metamodel Prediction Error of Optimal Specific Energy
 501 Absorption using Isotropic Material Model (UWR4)

502

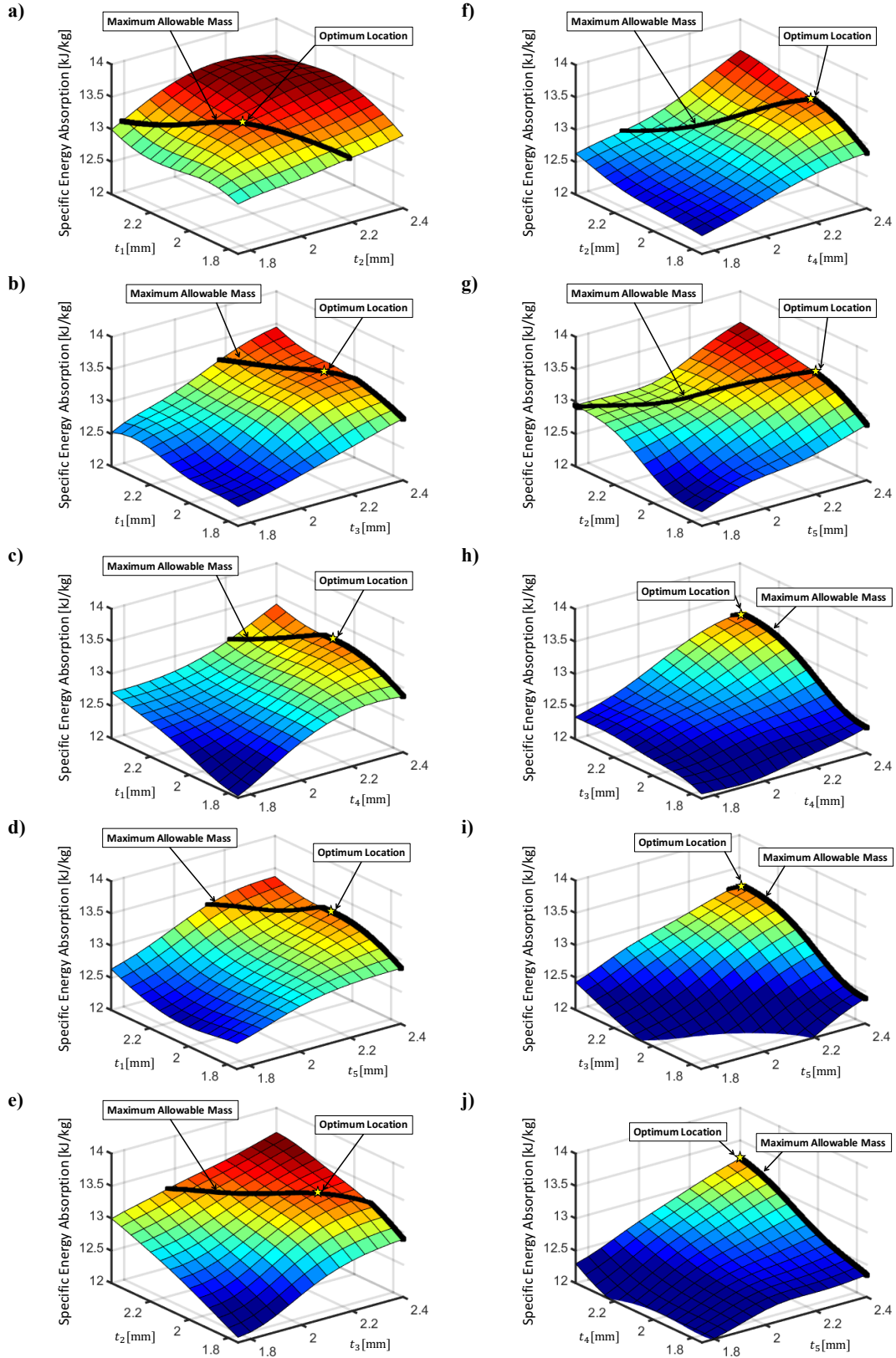


Figure 16 –Response surface response plots for specific energy absorption (SEA) of isotropic optimization process

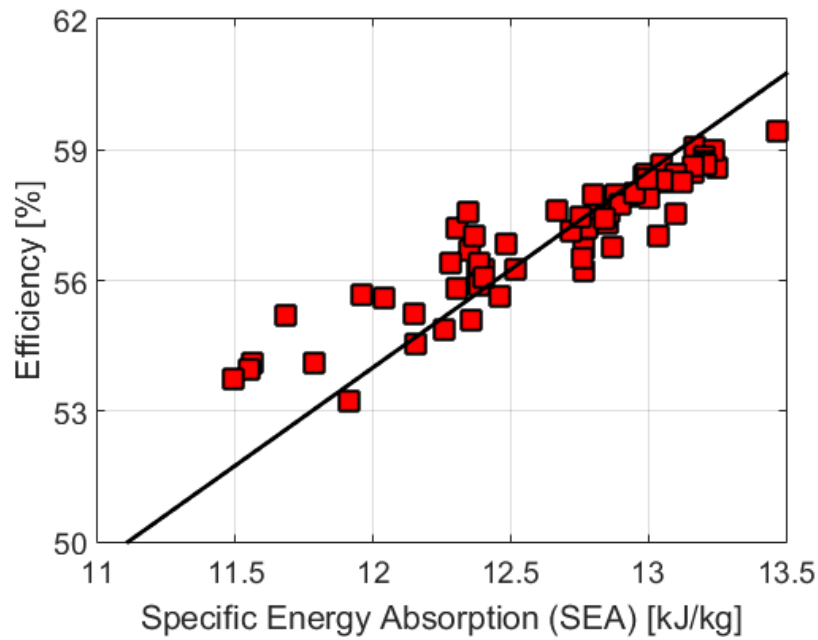


Figure 17 – Interaction of Specific Energy Absorption with Crush Efficiency for Isotropic procedure

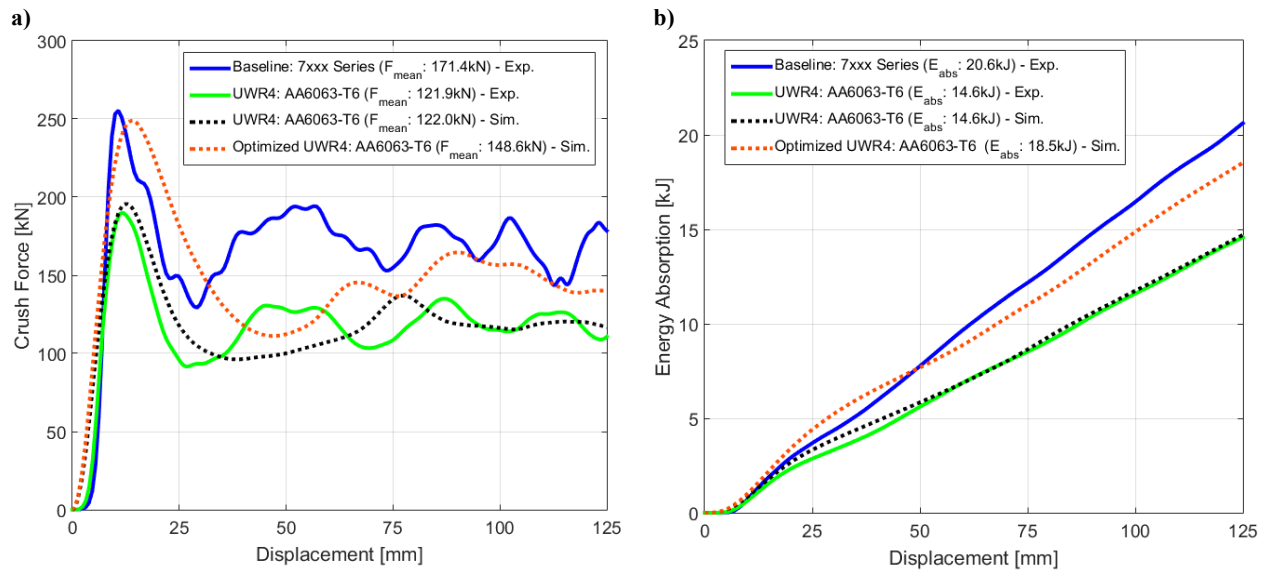


Figure 18 – Comparison of (a) Force-Displacement Response and (b) Energy Absorption Response for Baseline 7xxx Series Profile, UWR4 AA6063-T6 profile and new UWR4 AA6063-T6

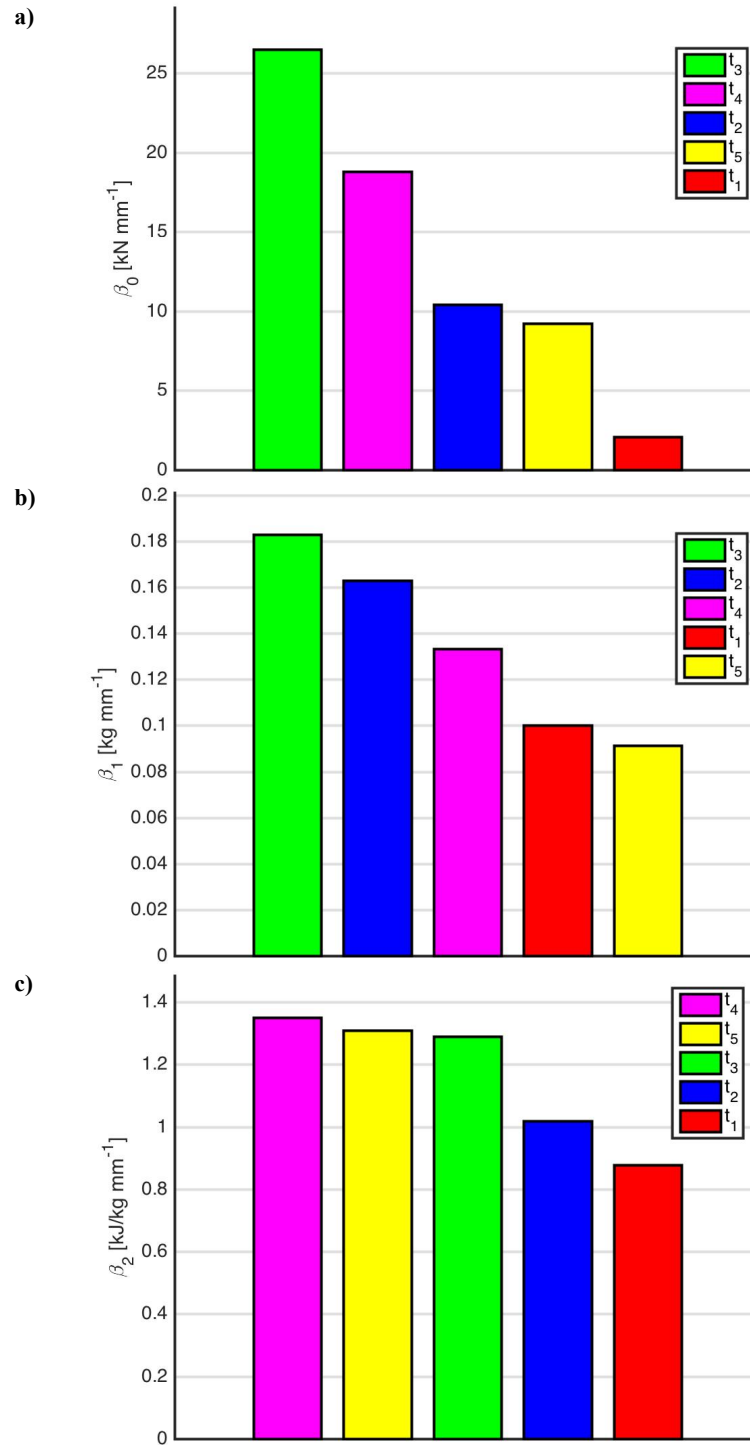


Figure 19 – (a) Mean Crush Force, (b) Mass, and (c) SEA Wall Thickness Sensitivity Analysis for New UWR4 AA6063-T6 profile

List of Tables

Table 1 – Extrusion Length, Mass and Specific Length of 7xxx Series and 6063 Extrusions

	Length [mm]	Mass [g]	Specific Length [g/mm]
Baseline 7xxx Profile	464	1494	3.22
Baseline AA6063-T6 profile	464	1295	2.79
UW-R4 AA6063-T6 profile	464	1234	2.66

Table 2 - Chemical composition of extrusion AA6063 aluminum alloy (wt%)

Al	Mg	Mn	Fe	Si	Cu	Ti
Bal	0.490	0.029	0.160	0.400	0.010	0.010

Table 3 – Power-law hardening parameters for the extruded AA6063 aluminum alloy

AA6063-T6	
K [MPa]	310
n	0.125
ε_0	0.0022

Table 4 – Summary of Experimental Crush Response for Profiles

	Baseline Profile 7xxx Series	Baseline Profile AA6063-T6	UWR4 Profile AA6063-T6
Energy Absorption [kJ]	20.6	11.0	14.6
Mean Crush Force [kN]	171.4	92.5	121.9
Peak Crush Force [kN]	255.4	161.4	190.0
Crush Efficiency [%]	67.1	57.3	64.2

Table 5 – Experimental Lankford Coefficients and Yield Stress Variation [37]

R_{00}	R_{45}	R_{90}	σ_{00}	σ_{45}	σ_{90}	R_b	σ_b
0.5667	0.3400	2.8567	226.556	207.068	195.88	0.4800	226.556

Table 6 – Elastic material properties of aluminum and steel

	Aluminum	Steel
Density [g/cm ³]	2.70	7.80
Elastic Modulus [MPa]	67900	205000
Poisson Ratio	0.34	0.30

Table 7 – Numerical, simulation and error for mean crush force, peak crush force, energy absorption and crush efficiency for Baseline AA6063-T6 Profile

	Energy Absorption, E_{abs} [kJ]	Mean Crush Force, F_{mean} [kN]	Peak Crush Force, F_{peak} [kN]	Crush Efficiency
Exp.	11.0	92.5	161.4	57.3
Sim. Prediction	10.7	85.5	151.8	56.3
ΔErr Exp. To Sim. (%)	2.7	7.6	5.9	1.0

Table 8 – Numerical, simulation and error for mean crush force, peak crush force, energy absorption and crush efficiency for UWR4 AA6063-T6 Profile

	Energy Absorption, E_{abs} [kJ]	Mean Crush Force, F_{mean} [kN]	Peak Crush Force, F_{peak} [kN]	Crush Efficiency
Exp.	14.6	121.9	190.0	64.2
Sim. Prediction	14.6	122.0	195.6	62.3
ΔErr Exp. To Sim. (%)	0.0	0.0	2.9	1.9

Table 9 – Initial and Final Topography and Mass

	Initial UWR4 AA6063-T6 Profile	New UWR4 AA6063-T6 Profile
t_1 [mm]	1.82	2.03
t_2 [mm]	1.85	1.97
t_3 [mm]	2.09	2.31
t_4 [mm]	1.80	2.40
t_5 [mm]	1.88	2.40
Mass [kg]	1.234	1.494

Table 10 – Regression Analysis of the Relationship between Crush Efficiency and Specific Energy Absorption

	Model
Regression Fit Slope \tilde{m} $\left[\frac{kJ/kg}{\%}\right]$	4.50
R^2 Fitting Result	0.6013
γ , $\left[\frac{kJ/kg}{\%}\right]$	4.20
Difference Between γ and \tilde{m} [%]	6.7

Table 11 – Summary of Energy Absorption Characteristics of New UWR4 AA6063 Profile

	Baseline 7xxx Series – Exp.	UWR4 AA6063- T6 – Exp.	UWR4 AA6063-T6 – Sim.	New UWR4 AA6063-T6 – Sim.	Gains of New UWR4 vs Baseline UWR4
Energy Absorption [kJ]	20.6	14.6	14.6	18.5	+26.7%
Mean Crush Force [kN]	171.4	121.9	122.0	148.6	+21.9%
Peak Crush Force [kN]	255.4	190.0	195.6	248.9	+27.2%
Crush Efficiency [%]	67.1	64.2	62.3	59.7	-2.5%
Mass [kg]	1.494	1.234	1.234	1.494	+21.0%